3D COMPRESSIBLE MELT TRANSPORT WITH MESH ADAPTIVITY

JULIANE DANNBERG[1,2], TIMO HEISTER[3]
[1] DANNBERG@MATH.TAMU.EDU, DEPARTMENT OF MATHEMATICS, TEXAS A&M UNIVERSITY, MAILSTOP 3368, COLLEGE STATION, TX 77843-3368, USA
[2] GEODYNAMIC MODELING, GFZ GERMAN RESEARCH CENTRE FOR GEOSCIENCES, POTSDAM, GERMANY
[3] HEISTER@CLEMSON.EDU, MATHEMATICAL SCIENCES, CLEMSON UNIVERSITY, SC 29634-0975, USA

ABSTRACT. Melt generation and migration are important processes for the evolution of the Earth's interior and impact the global convection of the mantle. While they have been the subject of numerous investigations, the typical time and length-scales of melt transport are vastly different from global mantle convection, which determines where melt is generated. This makes it difficult to study mantle convection and melt migration in a unified framework. The equations that describe coupled Stokes-Darcy flow have been derived a long time ago and they have been successfully implemented and applied in numerical models. However, modeling magma dynamics poses the challenge of highly non-linear and spatially variable material properties, in particular the viscosity. In addition, previous models neglected the individual compressibilities of the solid and the fluid phase. However, experiments have shown that the melt density change from the depth of melt generation to the surface leads to a volume increase of up to 20%. Considering these volume changes in both phases also ensures self-consistency of models that strive to link melt generation to processes in the deeper mantle, where the compressibility of the solid phase becomes more important. Here, we describe our extension of the finite element mantle convection code ASPECT that adds equations describing the behavior of silicate melt percolating through and interacting with a viscously deforming host rock. We use the original compressible formulation of the McKenzie equations, augmented by an equation for the conservation of energy. This approach includes both melt migration and melt generation with the accompanying latent heat effects. Applying adaptive mesh refinement to this type of problems is particularly advantageous, as the resolution can be increased in mesh cells where melt is present and viscosity gradients are high, whereas a lower resolution is sufficient in regions without melt. Together with a high-performance, massively parallel implementation, this allows for high resolution, 3d, compressible, global mantle convection simulations coupled with melt migration. We evaluate the functionality and potential of this method using a series of benchmarks and model setups relevant for applications, compare results of the compressible and incompressible formulation and show the effectiveness of adaptive mesh refinement when applied to melt migration. Our model of magma dynamics provides a framework for modeling processes on different scales and investigating links between processes occurring in the deep mantle and melt generation and migration. This approach could prove particularly useful applied to modeling the generation of komatiites or other melts originating in greater depths. The ASPECT code, including all presented modifications, is available online under an Open Source license[1]

1. INTRODUCTION

Mantle convection and melt migration are important processes for our understanding of the physics of the Earth's interior and how it is linked to observations at the surface. Both processes have been studied in much detail individually, however, most studies of solid-state creep in the Earth's mantle such as in mantle plumes, subduction zones or mantle convection in general either do not consider melting and melt migration, or treat it in a simplified way, only computing the melting rate and extracting the melt from the model, neglecting [e.g. 32, 2, 11, and references therein] or approximating [25, 29, 8, 20] the physics of two-phase flow and the effects of compaction. Previous modeling studies of magma dynamics comprise a wide range of applications, such as solitary waves [31], channeling instabilities [38], rifting [28], mid-ocean ridges [33, 14, 15], melt shear bands in partially molten rocks [34, 13] and magma dynamics in a host rock undergoing both fracture and flow [17]. However, these models often do not include the feedback of the melt on the solid mantle flow, they have only been carried out in two dimensions, and although they take into account the compaction of the solid matrix by changes in melt fraction, they treat both individual phases as incompressible.

These simplifications are valid on small scales, but become more limiting when linking surface observation to the deeper mantle and studying the interaction of mantle and magma dynamics in the context of larger-scale structures such as mantle plumes, subduction zones, and mid-ocean ridges. Typical compressibilities of mantle melts are in a range of $3.1 \cdot 10^{-11}$ to $5.3 \cdot 10^{-11}$Pa^{-1} [1, 21, 37, 26], implying that their volume can increase 7–11% per 100 km they ascend from the melting region. This volume change is especially important for melt generated in greater depths, such as komatiites.

Moreover, the geometry of geologic structures is not limited to two dimensions, examples being transform faults at mid-ocean ridges, plate velocities and lateral variations in the thickness of the overlying plate when a mantle plume impinges on the base of the lithosphere, and bent subduction zones or along-trench variations of oceanic crustal thickness. The three-dimensional structure of these settings has implications for the processes of melt migration, focusing and distribution of melt, and eventually the associated volcanism at the surface.

Nevertheless, several numerical challenges have prevented joint modeling of coupled magma and mantle dynamics in three dimensions so far: (1) Melt migration and mantle convection occur on widely different time and length scales, which makes it very difficult to study both processes together, as melt migration can only be resolved on a much higher resolution and using smaller time steps. (2) Important material properties strongly depend on temperature, pressure and in particular the porosity, leading for example to high viscosity contrasts of potentially more than 5 orders of magnitude often on very small length scales, which poses a challenge for iterative solvers. (3) These dependencies of the material parameters on the solution variables are strongly nonlinear, calling for advanced nonlinear solvers. All the previous points combined make it impossible to study these processes without using advanced numerical techniques and the ability to do large-scale parallel computations. We address these challenges in the following way:

(1) Adaptive mesh refinement allows us to refine the mesh where melt is present and viscosity contrasts are high, and to use a coarser mesh in regions without melt, where velocities and gradients of material properties are lower. For reaching the same accuracy overall fewer degrees of freedom and computational resources are required compared to a model with uniform mesh.
(2) Parallelization of the code, scaling up to 10,000s of processors makes it possible to run models with several tens of millions of degrees of freedom, allowing for large-scale models in three dimensions that still resolve processes on the length scale of melt migration.
(3) We use an iterated IMplicit Pressure Explicit Saturation (IMPES) scheme to resolve the strong non-linearity in the system, alternating the solution of the Stokes system and the advection systems until convergence is reached. We employ a generalized minimal residual method with a Wathen style block preconditioner for the Stokes part of the problem, allowing for high local and global viscosity contrasts.

The melt migration is integrated into the open source mantle convection code ASPECT [18, 4], which is based on the deal.II finite element library ([5]). The massively parallel, adaptive computing capabilities of the underlying deal.II library ([3]) enable the computations done for this paper.

Here, we present our extension of ASPECT that models coupled magma/mantle dynamics in two and three dimensions, employing adaptive mesh refinement. It includes all of the terms of the original formulation of two-phase flow of McKenzie [19], taking into account the compressibility of both individual phases, which makes this formulation (hereafter called fully compressible formulation) consistent also for higher pressures. Moreover, energy conservation, pressure-, temperature- and composition-dependent melt generation and latent heat effects are considered. We demonstrate the correctness and accuracy of the code by showcasing several benchmarks and convergence tests (Sections 4.1 and 4.3). Moreover, we show the effectiveness of adaptive mesh refinement using a test case that features structures expected in applications, but has an analytical solution (Sections 4.4). Finally, we present two- and three-dimensional application cases in earth-like settings, including mantle plumes, global mantle convection and magmatic shear bands (Sections 4.2, 4.5 and 4.6). The code used to generate these results is available online [9], and required input files, data files, and scripts for creating the analytic solutions are provided in the Supplementary Material.

TABLE 1. Explanation of some important symbols used in the paper.

Symbol	Quantity	Expression	Unit
ϕ	porosity		volume fraction
p_f	fluid pressure	$p_f = p_s - \frac{p_c}{1-\phi}$	Pa
p_s	solid pressure	$p_s = p_f + \frac{p_c}{1-\phi}$	Pa
p_c	compaction pressure	$p_c = (1-\phi)(p_s - p_f)$ $p_c = -\xi(\nabla \cdot \mathbf{u}_s)$	Pa
$\mathbf{u}_s$	solid velocity		m/yr
$\mathbf{u}_f$	fluid velocity	$\mathbf{u}_f = \mathbf{u}_s - \frac{K_D}{\phi}(\nabla p_f - \rho_f \mathbf{g})$	m/yr
$\dot{\varepsilon}$	strain rate	$\dot{\varepsilon}(\mathbf{u}_s) = \frac{1}{2}(\nabla \mathbf{u}_s + \nabla \mathbf{u}_s^T)$	1/yr
η	shear viscosity (solid)		Pa s
ξ	bulk viscosity (solid)		Pa s
η_f	shear viscosity (melt)		Pa s
K_D	Darcy coefficient	$K_D = \frac{k_\phi}{\eta_f}$	Pa

2. PROBLEM SETUP

2.1. **Physical model.** The original ASPECT mantle convection code [18] models the movement of solid mantle material. These computations also allow for taking into account how partially molten material changes the material properties and the energy balance through the release of latent heat. However, this does not include melt extraction or any relative movement between melt and solid. Here, we adapt ASPECT to solve additional equations describing the behavior of silicate melt percolating through and interacting with a viscously deforming host rock. This is implemented based on the approach of [17] in the viscous limit, extended to a compressible formulation.

Our model includes two material phases: The solid matrix (denoted with index s) and the fluid melt phase (denoted with index f). The melt fraction ϕ defines averaged quantities $\bar{X}$ out of solid (X_s) and fluid (X_f) quantities:

$$\bar{X} = (1-\phi)X_s + \phi X_f. \tag{1}$$

We start from the McKenzie equations, which are derived in Appendix A of [19]. The mass and momentum conservation for solid and fluid are:

$$\frac{\partial}{\partial t}\left[\rho_f \phi\right] + \nabla \cdot \left[\rho_f \phi \mathbf{u}_f\right] = \Gamma, \tag{2}$$

$$\frac{\partial}{\partial t}\left[\rho_s (1-\phi)\right] + \nabla \cdot \left[\rho_s (1-\phi)\mathbf{u}_s\right] = -\Gamma, \tag{3}$$

$$\phi\left(\mathbf{u}_f - \mathbf{u}_s\right) = -K_D\left(\nabla p_f - \rho_f \mathbf{g}\right), \tag{4}$$

$$-\nabla \cdot \left[2\eta\left(\dot{\varepsilon}(\mathbf{u}_s) - \frac{1}{3}(\nabla \cdot \mathbf{u}_s)\mathbf{1}\right) + \xi(\nabla \cdot \mathbf{u}_s)\mathbf{1}\right] + \nabla p_f = \bar{\rho}\mathbf{g}, \tag{5}$$

where ρ is the density (with the index denoting solid or fluid phase), $\mathbf{g}$ is the gravitational acceleration, Γ is the melting rate, and the other symbols are as given in Table 1. In order to eliminate the time derivatives, and under the assumption that the flow field is in equilibrium ($\partial \rho_{s,f}/\partial t = 0$), we rewrite the first two equations to:

$$\frac{\partial \phi}{\partial t} + \nabla \cdot \left[\phi \mathbf{u}_f\right] = \frac{\Gamma}{\rho_f} - \frac{\phi}{\rho_f}\mathbf{u}_f \cdot \nabla \rho_f, \tag{6}$$

$$-\frac{\partial \phi}{\partial t} + \nabla \cdot \left[(1-\phi)\mathbf{u}_s\right] = -\frac{\Gamma}{\rho_s} - \frac{1-\phi}{\rho_s}\mathbf{u}_s \cdot \nabla \rho_s. \tag{7}$$

Now we can add (6) and (7) and get

$$\nabla \cdot [\phi \mathbf{u}_f + (1-\phi)\mathbf{u}_s] = \Gamma \left(\frac{1}{\rho_f} - \frac{1}{\rho_s} \right) - \frac{\phi}{\rho_f} \mathbf{u}_f \cdot \nabla \rho_f - \frac{1-\phi}{\rho_s} \mathbf{u}_s \cdot \nabla \rho_s. \tag{8}$$

To eliminate the fluid velocity $\mathbf{u}_f$ from the equations, we replace it by using Darcy's law (Equation 4):

$$\phi \mathbf{u}_f = \phi \mathbf{u}_s - K_D \left(\nabla p_f - \rho_f \mathbf{g} \right) \tag{9}$$

and get

$$\begin{aligned} \nabla \cdot \mathbf{u}_s - \nabla \cdot [K_D (\nabla p_f - \rho_f \mathbf{g})] = \Gamma & \left(\frac{1}{\rho_f} - \frac{1}{\rho_s} \right) \\ & - \frac{\phi}{\rho_f} \mathbf{u}_s \cdot \nabla \rho_f + \frac{K_D}{\rho_f} \left(\nabla p_f - \rho_f \mathbf{g} \right) \cdot \nabla \rho_f \\ & - \frac{1-\phi}{\rho_s} \mathbf{u}_s \cdot \nabla \rho_s. \end{aligned} \tag{10}$$

Rearranging terms, we get

$$\begin{aligned} \nabla \cdot \mathbf{u}_s - \nabla \cdot K_D \nabla p_f - K_D \nabla p_f \cdot \frac{\nabla \rho_f}{\rho_f} = & -\nabla \cdot (K_D \rho_f \mathbf{g}) \\ & + \Gamma \left(\frac{1}{\rho_f} - \frac{1}{\rho_s} \right) \\ & - \frac{\phi}{\rho_f} \mathbf{u}_s \cdot \nabla \rho_f - \frac{1-\phi}{\rho_s} \mathbf{u}_s \cdot \nabla \rho_s \\ & - K_D \mathbf{g} \cdot \nabla \rho_f \qquad \text{in } \Omega. \end{aligned} \tag{11}$$

To avoid the density gradients, we can assume that the change in density (for both the solid and the fluid phase) is dominated by the change in static pressure, which can be written as $\nabla p_{s,f} \approx \nabla p_{\text{static}} \approx \rho_{s,f} \mathbf{g}$. This finally allows us to write

$$\frac{1}{\rho_{s,f}} \nabla \rho_{s,f} \approx \frac{1}{\rho_{s,f}} \frac{\partial \rho_{s,f}}{\partial p_{s,f}} \nabla p_{s,f} \approx \frac{1}{\rho_{s,f}} \frac{\partial \rho_{s,f}}{\partial p_{s,f}} \nabla p_{\text{static}} \approx \frac{1}{\rho_{s,f}} \frac{\partial \rho_{s,f}}{\partial p_{s,f}} \rho_{s,f} \mathbf{g} = \kappa_{s,f} \rho_{s,f} \mathbf{g}, \tag{12}$$

where $\kappa_{s,f}$ are the compressibilities of solid and fluid, respectively. We can now replace Equation (11) by

$$\begin{aligned} \nabla \cdot \mathbf{u}_s - \nabla \cdot K_D \nabla p_f - K_D \kappa_f \rho_f \nabla p_f \cdot \mathbf{g} = & -\nabla \cdot (K_D \rho_f \mathbf{g}) \\ & + \Gamma \left(\frac{1}{\rho_f} - \frac{1}{\rho_s} \right) \\ & - (\mathbf{u}_s \cdot \mathbf{g}) \left[\phi \kappa_f \rho_f + (1-\phi) \kappa_s \rho_s \right] \\ & - K_D \kappa_f \rho_f^2 \mathbf{g} \cdot \mathbf{g}. \end{aligned} \tag{13}$$

The original McKenzie formulation of the momentum equation (Equation 5, Equations (A16) - (A18) in [19]) only contains the fluid pressure. However, analogous to [17] we can define a new variable, the compaction pressure, as

$$p_c = (1-\phi)(p_s - p_f).$$

The viscous constitutive law for the compaction stress in the host rock (see [17], viscous limit) is

$$p_c = -\xi (\nabla \cdot \mathbf{u}_s), \tag{14}$$

which allows us to replace the compaction term in (5) by the compaction pressure:

$$-\nabla\cdot\left[2\eta\left(\dot{\varepsilon}(\mathbf{u}_s)-\frac{1}{3}(\nabla\cdot\mathbf{u}_s)\mathbf{1}\right)\right]+\nabla p_f+\nabla p_c=\bar{\rho}\mathbf{g}. \tag{15}$$

The final set of equations are (15), (13) and (14):

$$\begin{aligned}
-\nabla\cdot\left[2\eta\left(\dot{\varepsilon}(\mathbf{u}_s)-\frac{1}{3}(\nabla\cdot\mathbf{u}_s)\mathbf{1}\right)\right]+\nabla p_f+\nabla p_c &= \bar{\rho}\mathbf{g},\\
\nabla\cdot\mathbf{u}_s-\nabla\cdot K_D\nabla p_f-K_D\kappa_f\rho_f\nabla p_f\cdot\mathbf{g} &= -\nabla\cdot(K_D\rho_f\mathbf{g})\\
&\quad+\Gamma\left(\frac{1}{\rho_f}-\frac{1}{\rho_s}\right)\\
&\quad-(\mathbf{u}_s\cdot\mathbf{g})\left[\phi\kappa_f\rho_f+(1-\phi)\kappa_s\rho_s\right]\\
&\quad-K_D\kappa_f\rho_f^2\mathbf{g}\cdot\mathbf{g},\\
\nabla\cdot\mathbf{u}_s+\frac{p_c}{\xi} &= 0.
\end{aligned}$$

The equations are solved for the solid velocity $\mathbf{u_s}$, the fluid pressure p_f, and the compaction pressure p_c. Without the presence of melt ($\phi = 0$), the equations reduce to the standard compressible Stokes system used in ASPECT. For the material properties used in the equations, there are many different parameterizations provided in the literature, so in ASPECT these material description can be set in a material model module that can be easily modified by the user, and we will use different formulations for the various models presented in this manuscript. Through the permeability, which is often parametrized as $k_\phi = k_0\phi^n$, the Darcy coefficient K_D depends on the solution variables, as well as the shear, and compaction viscosities η and ξ, which can depend on the porosity, temperature, pressure, strain rate and composition. Common formulations for the dependence on porosity are $\eta = (1-\phi)\eta_0 e^{-\alpha_\phi\phi}$ with $\alpha_\phi \approx 25...30$ and $\xi = \eta_0\zeta\phi^{-n}$ with $n \approx 1$ and $\zeta \approx 1...10$ [e.g. 14, 15, 17, and references therein]. These dependencies introduce strong non-linearities in the equations, which have to be considered when solving the system. Note that we use a three-field instead of a two-field system of equations here, based on the results of previous studies [22, 23] showing that the construction of a uniform preconditioner with respect to the model parameters is difficult for the two-field formulation, while preconditioners are less sensitive to these parameters for the three-field problem.

We use Dirichlet boundary conditions for the velocity and Neumann boundary conditions for the fluid pressure:

$$\mathbf{u}_s = \mathbf{f}_1 \text{ on } \partial\Omega, \tag{16}$$

$$\nabla p_f = \mathbf{f}_2 \text{ on } \partial\Omega. \tag{17}$$

Prescribing the lithostatic pressure gradient $\mathbf{f}_2 = \rho_s\mathbf{g}$ leads to melt flowing in only due to variations in the dynamic pressure, whereas $\mathbf{f}_2 = \rho_f\mathbf{g}$ together with $\mathbf{f}_1\cdot\vec{n} = 0$ leads to no in- and outflow of melt or solid. Arbitrary melt fluxes can be prescribed in addition to these options. Note that the compatibility condition implies $\int_\Omega \frac{p_c}{\xi}\,\mathrm{d}x = 0$.

Here, we do not use the visco-elasto-plastic rheology of the Keller et al. [17] formulation. Hence, we do not consider the elastic deformation terms that would appear on the right hand side of Equation 15 and Equation 14 and that include the elastic and compaction stress evolution parameters ξ_τ and ξ_p. Moreover, our viscosity parameters η and ξ only cover viscous deformation instead of combining visco-elasticity and plastic failure.

In addition to the previously derived conservation equations for total mass and momentum (Equations 13 – 15), melt transport requires an advection equation that governs the evolution of the porosity field ϕ and an equation for the conservation of energy. Under the assumption of equilibrium ($\partial\rho_{s,f}/\partial t = 0$) we can write Equation 3 as:

$$\rho_s\frac{\partial(1-\phi)}{\partial t}+\nabla\cdot[\rho_s(1-\phi)\mathbf{u}_s] = -\Gamma. \tag{18}$$

To bring this equation in the same form as the other advection equations in ASPECT, we replace the second term of the equation by

$$\nabla \cdot [\rho_s(1-\phi)\mathbf{u}_s] = (1-\phi)\left(\rho_s \nabla \cdot \mathbf{u}_s + \nabla\rho_s \cdot \mathbf{u}_s\right) - \nabla\phi \cdot \rho_s \mathbf{u}_s.$$

Then we use the same method as for the mass conservation and assume the change in density is dominated by the change in static pressure. This finally allows us to use Equation 12 to replace $\nabla\rho_s/\rho_s = \kappa_s\rho_s\mathbf{g}$ and write

$$\frac{\partial\phi}{\partial t} + \mathbf{u}_s \cdot \nabla\phi = \frac{\Gamma}{\rho_s} + (1-\phi)(\nabla \cdot \mathbf{u}_s + \kappa_s\rho_s\mathbf{g} \cdot \mathbf{u_s}). \tag{19}$$

In order to model melting and freezing of melt, we also need a solution for the temperature T and thus include an energy conservation equation in our model that includes radiogenic heat production, shear heating, adiabatic heating, and release and consumption of latent heat of melting/freezing:

$$\begin{aligned} \rho_s C_p \left(\frac{\partial T}{\partial t} + \mathbf{u}_s \cdot \nabla T\right) - \nabla \cdot k\nabla T = \rho_s H & \\ + 2\eta\left(\dot{\varepsilon_s} : \dot{\varepsilon_s}\right) & \\ + \alpha T\left(\mathbf{u}_s \cdot \nabla p_s\right) & \\ + T\Delta S\,\Gamma, & \end{aligned} \tag{20}$$

with the shear strain rate $\dot{\varepsilon_s} = \dot{\varepsilon}(\mathbf{u}_s) - \frac{1}{3}(\nabla \cdot \mathbf{u}_s)\mathbf{1}$. This formulation assumes thermal equilibrium in the whole model domain. As our emphasis is on the mechanical modeling, we do not include the effect of melt migration on the energy equation – except for the latent heat of melting and freezing $T\Delta S\,\Gamma$, which is determined by the entropy change ΔS upon melting the material completely and the melting rate Γ – and use phase-independent parameterizations for thermal expansivity α, specific heat C_p and thermal conductivity k.

2.2. **Weak formulation.** To apply the finite element method we need to derive the weak form of the equations (13), (14), and (15). We multiply by test functions, integrate over the domain, and integrate by parts:

$$(2\eta\dot{\varepsilon}(\mathbf{u}_s), \dot{\varepsilon}(\mathbf{v}_s)) - \frac{2}{3}\eta\left(\nabla \cdot \mathbf{u}_s, \nabla \cdot \mathbf{v}_s\right) + \left(\nabla p_f, \mathbf{v}_s\right) + \left(\nabla p_c, \mathbf{v}_s\right) = \left(\bar{\rho}\mathbf{g}, \mathbf{v}_s\right), \tag{21}$$

$$\begin{aligned} \left(\nabla \cdot \mathbf{u}_s, q_f\right) - \left(\nabla \cdot K_D\nabla p_f, q_f\right) - \left(K_D\kappa_f\rho_f\nabla p_f \cdot \mathbf{g}, q_f\right) = & -\left(\nabla \cdot (K_D\rho_f\mathbf{g}), q_f\right) \\ & + \left(\frac{1}{\rho_f} - \frac{1}{\rho_s}\right)\left(\Gamma, q_f\right) \\ & - \left[\phi\kappa_f\rho_f + (1-\phi)\kappa_s\rho_s\right]\left(\mathbf{u}_s \cdot \mathbf{g}, q_f\right) \\ & - \left(K_D\kappa_f\rho_f^2\mathbf{g} \cdot \mathbf{g}, q_f\right), \end{aligned} \tag{22}$$

$$\left(\nabla \cdot \mathbf{u}_s, q_c\right) + \left(\frac{1}{\xi}p_c, q_c\right) = 0. \tag{23}$$

For the first equation we do integration by parts on the pressure terms ($\mathbf{v} = 0$ on the boundary, so the boundary integral vanishes):

$$(2\eta\dot{\varepsilon}(\mathbf{u}_s), \dot{\varepsilon}(\mathbf{v}_s)) - \left(\frac{2}{3}\eta\nabla \cdot \mathbf{u}_s, \nabla \cdot \mathbf{v}_s\right) - \left(p_f, \nabla \cdot \mathbf{v}_s\right) - \left(p_c, \nabla \cdot \mathbf{v}_s\right) = \left(\bar{\rho}\mathbf{g}, \mathbf{v}_s\right). \tag{24}$$

We aim to include only material properties and not their derivatives in the equations, because these material descriptions are provided by ASPECT's user-defined plugins, which are designed to be easily comprehensible and extensible. Thus, we integrate the first part on the right hand side of the second equation by parts (and pick up a boundary term):

$$\left(\nabla \cdot (K_D\rho_f\mathbf{g}), q_f\right) = -\left(K_D\rho_f\mathbf{g}, \nabla q_f\right) + \int_\Gamma q_f K_D\rho_f\mathbf{g} \cdot \vec{n}\,\mathrm{d}s.$$

We reverse the sign to later have a symmetric system:

$$
\begin{aligned}
-\left(\nabla\cdot\mathbf{u}_s, q_f\right) + \left(\nabla\cdot K_D\nabla p_f, q_f\right) + \left(K_D\kappa_f\rho_f\nabla p_f\cdot\mathbf{g}, q_f\right) = &-\left(K_D\rho_f\mathbf{g}, \nabla q_f\right)\\
&+\int_\Gamma q_f K_D\rho_f\mathbf{g}\cdot\vec{n}\,\mathrm{d}s\\
&-\left(\frac{1}{\rho_f}-\frac{1}{\rho_s}\right)\left(\Gamma, q_f\right)\\
&+\left[\phi\kappa_f\rho_f + (1-\phi)\kappa_s\rho_s\right]\left(\mathbf{u}_s\cdot\mathbf{g}, q_f\right)\\
&+\left(K_D\kappa_f\rho_f^2\mathbf{g}\cdot\mathbf{g}, q_f\right).
\end{aligned}
\tag{25}
$$

The second term on the left needs to be integrated by parts to get

$$
\left(\nabla\cdot K_D\nabla p_f, q_f\right) = -\left(K_D\nabla p_f, \nabla q_f\right) + \int_\Gamma q_f K_D\nabla p_f\cdot\vec{n}\,\mathrm{d}s.
$$

We can use the boundary integral to prescribe Neumann boundary conditions for p_f (Equation 17), and with $\nabla p_f = \mathbf{f}_2$ on the boundary we can move the boundary term to the right-hand side and get:

$$
\int_\Gamma q_f K_D\rho_f\mathbf{g}\cdot\vec{n}\,\mathrm{d}s - \int_\Gamma q_f K_D\nabla p_f\cdot\vec{n}\,\mathrm{d}s = -\int_\Gamma q_f K_D(\rho_f\mathbf{g}-\mathbf{f}_2)\cdot\vec{n}\,\mathrm{d}s.
$$

For the third equation we also flip the sign to get

$$
-\left(\nabla\cdot\mathbf{u}_s, q_c\right) - \left(\frac{1}{\xi}p_c, q_c\right) = 0. \tag{26}
$$

Finally, the weak form reads:

$$
\begin{aligned}
\left(2\eta\dot{\varepsilon}(\mathbf{u}_s), \dot{\varepsilon}(\mathbf{v}_s)\right) - \left(\frac{2}{3}\eta\nabla\cdot\mathbf{u}_s, \nabla\cdot\mathbf{v}_s\right)&\\
-(p_f, \nabla\cdot\mathbf{v}_s) - (p_c, \nabla\cdot\mathbf{v}_s) = \left(\bar{\rho}\mathbf{g}, \mathbf{v}_s\right),&
\end{aligned}
\tag{27}
$$

$$
\begin{aligned}
-\left(\nabla\cdot\mathbf{u}_s, q_f\right) - \left(K_D\nabla p_f, \nabla q_f\right)&\\
+\left(K_D\kappa_f\rho_f\nabla p_f\cdot\mathbf{g}, q_f\right) = &-\left(K_D\rho_f\mathbf{g}, \nabla q_f\right)\\
&-\int_\Gamma q_f K_D(\rho_f\mathbf{g}-\mathbf{f}_2)\cdot\vec{n}\,\mathrm{d}s\\
&-\left(\frac{1}{\rho_f}-\frac{1}{\rho_s}\right)\left(\Gamma, q_f\right)\\
&+\left[\phi\kappa_f\rho_f + (1-\phi)\kappa_s\rho_s\right]\left(\mathbf{u}_s\cdot\mathbf{g}, q_f\right)\\
&+\left(K_D\kappa_f\rho_f^2\mathbf{g}\cdot\mathbf{g}, q_f\right),
\end{aligned}
\tag{28}
$$

$$
-\left(\nabla\cdot\mathbf{u}_s, q_c\right) - \left(\frac{1}{\xi}p_c, q_c\right) = 0. \tag{29}
$$

3. Discretization and Linear Solvers

Let $(\mathbf{u}_s, p_f, p_c) \in V^u \times V^{p_f} \times V^{p_c}$ be the continuous solutions of the weak form (27)–(29). While $V^u = \left[H_0^1(\Omega)\right]^d$ is natural (we assume homogeneous boundary conditions for simplicity here), the choice for V^{p_f} and V^{p_c} require more thought:

Unique solvability can only be expected with an additional normalization condition like $\int_\Omega p_f = 0$. If we assume $K_D > 0$ at all times, the natural space for the fluid pressure would be

$$
V^{p_f} = H_*^1(\Omega) = H^1(\Omega)\cap L_*^2(\Omega),
$$

while for $K_D = 0$ it reduces to $L^2_*(\Omega) = \{q \in L^2(\Omega) \mid \int_\Omega q = 0\}$ and we experience a standard inf-sup condition known from the Stokes equation.

Assuming ξ is finite, the constant in the compaction pressure p_c is already uniquely determined due to (29), which is essentially an L^2 projection of the divergence into p_c. The correct space here is $V^{p_c} = L^2(\Omega)$.

We now discretize using conforming finite elements on quadrilaterals. An example for a stable discretization is given by

$$V_h^u \times V_h^{p_f} \times V_h^{p_c} = Q_k^d \times Q_{k-1} \times Q_{k-1} \subset V^u \times V^{p_f} \times V^{p_c}$$

with $k \geq 2$ where Q_k is the standard continuous space of tensor-product polynomials of degree k on the reference cell. For $k = 2$ this results in the standard Taylor-Hood pair $Q_2^d \times Q_1$ for both velocity/pressure pairs. For the evolution of the melt fraction, we achieve the best results when choosing elements of degree $k - 1$ for the porosity field. In this case, the divergence of the velocity, which is contained in the advection equation as a source term, and the porosity are in the same function space, and no interpolation is necessary. This guarantees that no melt is generated for a divergence-free velocity field.

As we use stable finite elements, we do not have to impose a minimum permeability to avoid stability problems, which has been done in previous finite element magma dynamics implementations. Instead, there is a continuous transition to Stokes flow for zero porosity. Nevertheless, we have to limit the compaction viscosity for low porosities to guarantee $\xi < \infty$, which would technically be possible by setting $1/\xi = 0$ and, but would make Equations 28 and 29 linear dependent.

3.1. **Linear System.**

Discretizing (27)–(29), we obtain the linear system

$$\begin{pmatrix} \mathbf{A} & \mathbf{B}^T & \mathbf{B}^T \\ \mathbf{B} & \mathbf{N} & \mathbf{0} \\ \mathbf{B} & \mathbf{0} & \mathbf{K} \end{pmatrix} \begin{pmatrix} \mathbf{U}_s \\ \mathbf{P}_f \\ \mathbf{P}_c \end{pmatrix} = \begin{pmatrix} \mathbf{F} \\ \mathbf{G} \\ \mathbf{0} \end{pmatrix}. \tag{30}$$

Where $\mathbf{N}$ is the discretization of $(K_D \nabla p_f, \nabla q_f)$ in the incompressible case and $\mathbf{K}$ is given by $\left(\frac{1}{\xi} p_c, q_c\right)$. For compressible computations, $\mathbf{N}$ also contains the non-symmetric, third term from (28).

Based on the solver strategy in [23], we solve the block system (30) using flexible GMRES with the upper block triangular preconditioner (preconditioned from the right)

$$\mathbf{P}^{-1} = \begin{pmatrix} \mathbf{A} & \mathbf{B}^T & \mathbf{B}^T \\ \mathbf{0} & \mathbf{X} & \mathbf{0} \\ \mathbf{0} & \mathbf{0} & \mathbf{Y} \end{pmatrix}^{-1}.$$

For the Schur complement approximations we choose

$$\mathbf{X} = \mathbf{B}\mathbf{A}^{-1}\mathbf{B}^T + \mathbf{N} \approx \frac{1}{\eta}\mathbf{M}_{p_f} + K_D \mathbf{L}_{p_f} = \hat{\mathbf{X}}$$

and

$$\mathbf{Y} = \mathbf{B}\mathbf{A}^{-1}\mathbf{B}^T + \mathbf{K} \approx (\frac{1}{\eta} + \frac{1}{\xi})\mathbf{M}_{p_c} = \hat{\mathbf{Y}},$$

where $\mathbf{M}_*$ and $\mathbf{L}_*$ are mass and stiffness matrices, respectively. While the preconditioner $\mathbf{P}$ is only defined for constant coefficients this way, varying coefficients can be treated by pulling them into the integration for the mass and stiffness matrices in $\hat{\mathbf{X}}$ and $\hat{\mathbf{Y}}$.

The approximation for $\mathbf{A}^{-1}$ is done using an inner CG solver with a relative tolerance of 10^{-2} preconditioned by Trilinos ML applied to the diagonal blocks of $\mathbf{A}$. The Schur complement solves for $\hat{\mathbf{X}}^{-1}$ and $\hat{\mathbf{Y}}^{-1}$ are also done using CG preconditioned by a block ILU(0).

4. Numerical Results

In the following, we will demonstrate the accuracy and versatility of our code at the example of a number of benchmark cases and relevant setups for coupled magma/mantle dynamics applications.

4.1. **Incompressible solitary wave benchmark.** The support of non-linear solitary waves is a well-known feature of the melt migration equations, resulting from the ability of the solid matrix to compact and dilate [7, 6] and this problem has become a standard for benchmarking magma migration codes [31, 17, 27]. Moreover, solitary waves have been suggested as a way of magma transport in the mantle, contributing to its episodic behavior [30, 39]. For 1D solitary waves, assuming constant shear and compaction viscosities and using a permeability law in form of

$$k_\phi = k_0\phi^3, \qquad \text{implying a Darcy coefficient } K_D(\phi) = \frac{k_0}{\eta_f}\phi^3,$$

and the non-dimensionalization

$$\begin{aligned} x &= \delta x' && \text{with the compaction length } \delta = \sqrt{K_D(\phi_0)(\xi + \frac{4}{3}\eta)}, \\ \phi &= \phi_0\phi' && \text{with the background porosity } \phi_0, \\ (\mathbf{u}_s, \mathbf{u}_f) &= u_0(\mathbf{u}_s, \mathbf{u}_f)' && \text{with the separation flux } \phi_0 u_0 = K_D(\phi_0)\Delta\rho g, \\ t &= \frac{\delta}{u_0}t', \end{aligned}$$

there is an analytical solution for the shape of the solitary wave, which can be written in the implicit form:

$$x(\phi) = \pm(A + 0.5)\left[-2\sqrt{A-\phi} + \frac{1}{\sqrt{A-1}}\ln\frac{\sqrt{A-1}-\sqrt{A-\phi}}{\sqrt{A-1}+\sqrt{A-\phi}}\right],$$

with $A > 1$ being the non-dimensional amplitude of the wave [7]. When scaled back to physical units, this equation describes a wave with the amplitude A/ϕ_0 propagating with a fixed shape and constant phase speed $c = u_0(2A/\phi_0+1)$ in a uniform porosity ($\phi = \phi_0$) background. This is only valid in the limit of small porosity $\phi_0 \ll 1$.

For running this 1D benchmark problem, we use a pseudo-1-D profile with only a few elements in the horizontal direction and a vertical extension of 400 m, chosen in such a way that the deviation from background porosity $\phi/\phi_0 - 1 < 10^{-7}$. The resolution in this direction is varied as multiples of two of the coarsest grid with $n_z = 160$, resulting in a resolution of 2.5 m ... 0.3 m. We apply the negative phase speed of the solitary wave $\mathbf{u}_s = -c\,\mathbf{e}_z$ as velocity boundary condition, so that the wave will stay at its original position while the background is moving, and set the end time of the model to $t = 6 \cdot 10^6$ years to allow the wave to propagate five times its wavelength. The parameters used for the model are taken from Keller et al. [17] and are given in Table 2. Figure 1 displays the shape of the solitary wave for both porosity and compaction pressure in the final time step for different models as well as the analytical solution.

We evaluate the accuracy of our model results by comparing both the phase speed and the shape of the wave after the model runtime to this analytical solution. In order to do this, we calculate the deviation of the position of the computed wave from the analytical solution (the phase shift Δz). This is done by averaging over the the distance between points with the same porosity in both solutions:

$$\Delta z = \sum_{\phi=\phi_0}^{A/\phi_0} \frac{z_{num}(\phi) - z_{ana}(\phi)}{n}.$$

We can then use the phase shift to calculate the phase speed error

$$e_c = \left|\frac{c_{num}}{c_{ana}} - 1\right|$$

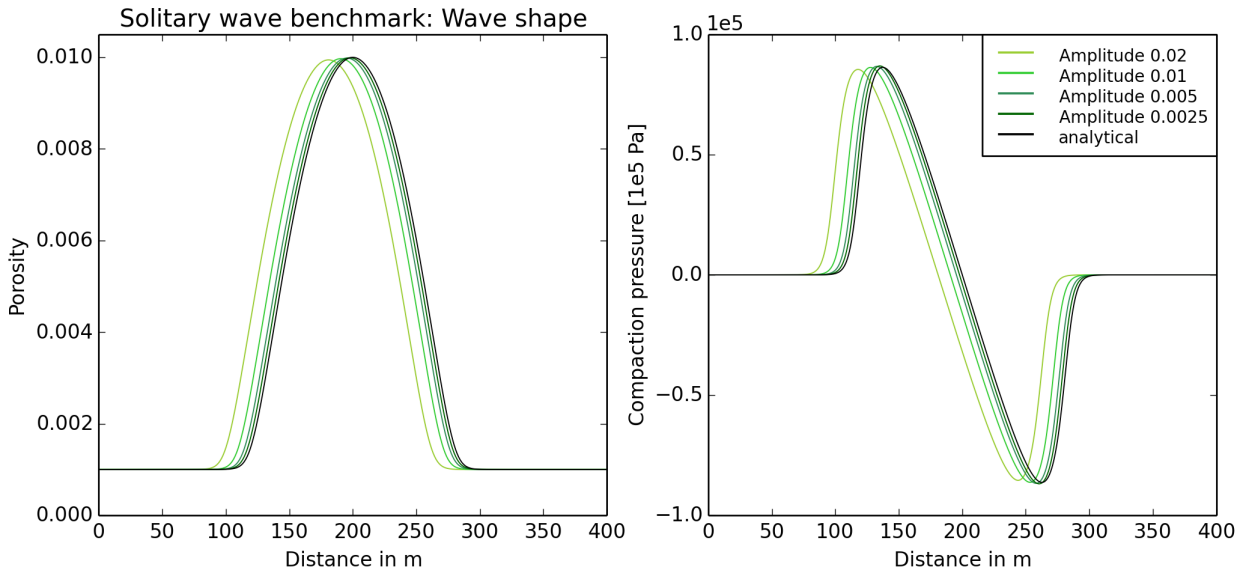

FIGURE 1. *Shape of the solitary wave in porosity (left) and compaction pressure (right) for the same resolution, but different wave amplitudes, still retaining the same non-dimensional problem, after propagating five times its wave length. The porosity is scaled according to the wave amplitude to make the plots comparable, and the end time of each model is chosen according to the phase speed of the wave (proportional to the wave amplitude) with a model time of* $t = 6 \cdot 10^6$ *years for* $A = 0.01$. *Both porosity and compaction pressure illustrate how the model result approaches the analytical solution with decreasing porosity.*

and the porosity and pressure shape errors

$$e_\phi = \frac{\|\phi_{num}(z) - \phi_{ana}(z - \Delta z)\|_2}{A},$$
$$e_p = \frac{\|p_{c_{num}}(z) - p_{c_{ana}}(z - \Delta z)\|_2}{A_p}.$$

Figure 2 illustrates the time evolution of these errors for simulations with different resolutions and time step sizes. After an initial transient stage, the shape and phase speed errors remain constant. This demonstrates that the code is able to capture the expected behavior of a solitary wave that moves with a constant phase speed without changing its shape. However, the errors do not seem to converge to zero with increasing resolution. This is expected, as solitary waves are the solution of a simplified formulation of the porous flow equations that is only valid in the limit of small porosity. To show how the solution depends on the amplitude of the wave A and the background porosity ϕ_0, we performed a series of models with the same parameters as given in Table 2, but varying ϕ_0, and accordingly changed the reference permeability, background velocity and maximum porosity A/ϕ_0 to retain the same non-dimensional problem, only modifying the scaling. The results (Figure 3) show that all errors decrease with decreasing porosity. This is also visible in Figure 1, where the shape of the solitary wave approaches the one of the analytical solution for small wave amplitudes. The results show no dependence on time step size (Figure 2), and we attribute this to the fact that the position of the solitary wave – and the numerical solution for each time step – only changes very slowly with time because we prescribe the negative wave speed at the model boundaries.

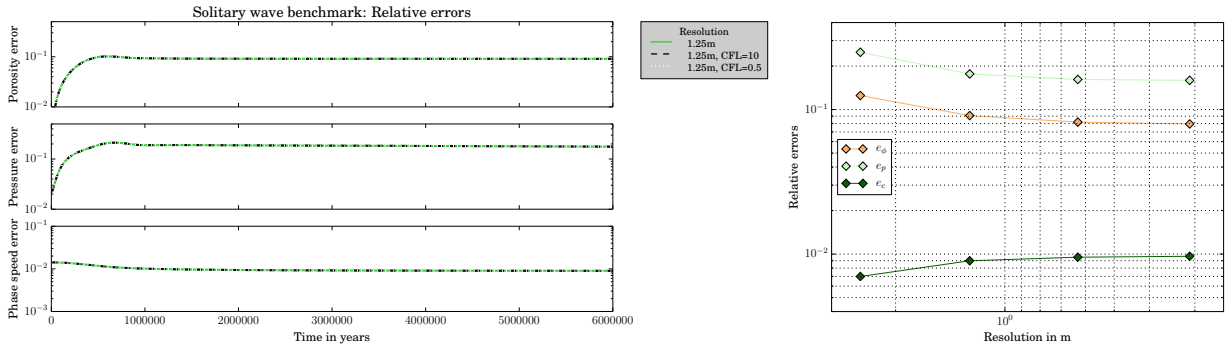

FIGURE 2. *Results of temporal (left) and spatial (right) convergence tests, plotted are the errors of the porosity e_ϕ, compaction pressure e_p and phase speed e_c relative to the 1-D analytical solution against model time and resolution, respectively. Grid resolution is chosen as multiples of two of the coarsest grid with 160 grid cells in vertical direction, corresponding to a cell size of $2.5\,m$ ... $0.3\,m$ or approximately $1/80...1/640$ of the wavelength of the solitary wave. Time step lengths are chosen according to the CFL condition for the respective phase speed c.*

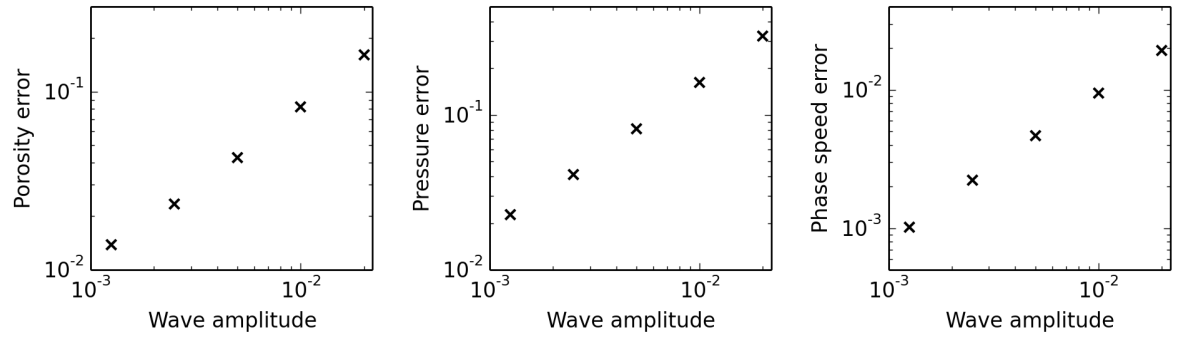

FIGURE 3. *Accuracy of the solution in dependence of the solitary wave amplitude resp. background porosity. Plotted are the shape error of porosity (left), compaction pressure (middle) and the phase speed error (right) in the final time step compared to the 1-D analytical solution. All model runs are performed with a grid resolution of 0.625 m and the model end time is inversely proportional to the wave speed (proportional to the wave amplitude) with a model time of $t = 6 \cdot 10^6$ years for $A = 0.01$. All errors converge to zero as the porosity approaches zero.*

4.2. **Magmatic shear bands.** It has been suggested and shown both numerically and experimentally that shear bands are a typical feature emerging when simple shear is applied to a partially molten rock [36, 12]. These shear bands are predicted to grow fastest under an angle of 45° to the orientation of highest shear stress if the rheology of the host rock is Newtonian and porosity-dependent [34], but to develop at much smaller angles in case of a combination of porosity-dependent and power-law viscosity [13]. We present shear band models analogous to the setup of [13], using a power-law relation in the form

$$\eta(\phi, \dot{\varepsilon}) = \eta_0 e^{\alpha(\phi-\phi_0)} \dot{\varepsilon}_{II}^{\frac{1-n}{n}} \tag{31}$$

TABLE 2. Parameters and scaling used for the solitary wave benchmark.

Symbol	Expression
ξ	10^{20} Pa s
η	10^{20} Pa s
η_f	100 Pa s
ρ_{s_0}	3000 kg/m^3
ρ_{f_0}	2500 kg/m^3
k_0	5×10^{-9} m^2
ϕ_0	1^{-3} (convergence tests)
	$2.5^{-4}...2^{-3}$ (porosity-dependence)
A	10
δ_0	3.41565 m
u_0	2.5×10^{-13} m/s= 7.8894×10^{-6} m/yr
c	1.656774×10^{-4} m/yr
CFL	1, 0.5, 0.25, 0.125
n_z	160, 320, 640, 1280
resolution	2.5 m, 1.25 m, 0.625 m, 0.3125 m

for both the porosity and strain rate dependence of viscosity with an exponent of $\alpha = -27$ for the porosity and $n = 6$ for the strain rate. The permeability is parametrized using the common formulation $k_\phi = k_0\phi^3$. The model geometry is a 4 mm $\times$ 1 mm 2D box periodic in the horizontal direction, starting from a background porosity $\phi_0 = 0.05$ with a white noise perturbation with an amplitude of 0.0005. A constant horizontal velocity $u_s = (\pm 32\,\text{m yr}^{-1}, 0)$ in opposite directions is applied at the top and bottom boundaries, leading to a strain rate of $\dot{\varepsilon} = 1.434\,\text{s}^{-1}$, and the vertical gradients of pressure and porosity are required to be zero at these boundaries. A comprehensive list of model parameters and the material description can be found in Table 3. During the model evolution, elongated melt bands develop due to the applied shear; and we measure the angle of these bands after a strain of $\gamma = 1$ is reached (Figure 4, top). We apply a Fourier transform to the porosity field of the final time step and analyze the amplitude of the resulting frequencies in dependence of their angle. Figure 4 (middle left) shows a histogram of these values binned by band angle. The average angle of the shear bands is then computed by fitting a log-normal to the band angle distribution. Computations with varying resolutions (Figure 4, middle right) show that the band angle converges to a value of approximately 17.5°, being in the range of predictions from experiments and other numerical models, where 15° – 25° to the plane of shear are reported [13]. A model of magmatic shear bands in three dimensions, but otherwise identical setup (Figure 4, bottom) reveals that the modeled shear bands are indeed planar features also in 3D. They still emerge in a certain angle determined by the applied shear, while the white noise – initially randomly distributed in all three dimensions – only modulates the concentration of porosity in the band along its extension. The model has a resolution of 8 μm, which corresponds to 45 million degrees of freedom, and the full model evolution is shown in Supplementary Movie S1.

4.3. **Compressible convergence.** To set up a 2D test for melt transport including compressiblity, we developed a new benchmark with an analytical solution, choosing the velocity, density and gravity in such a way that the laterally

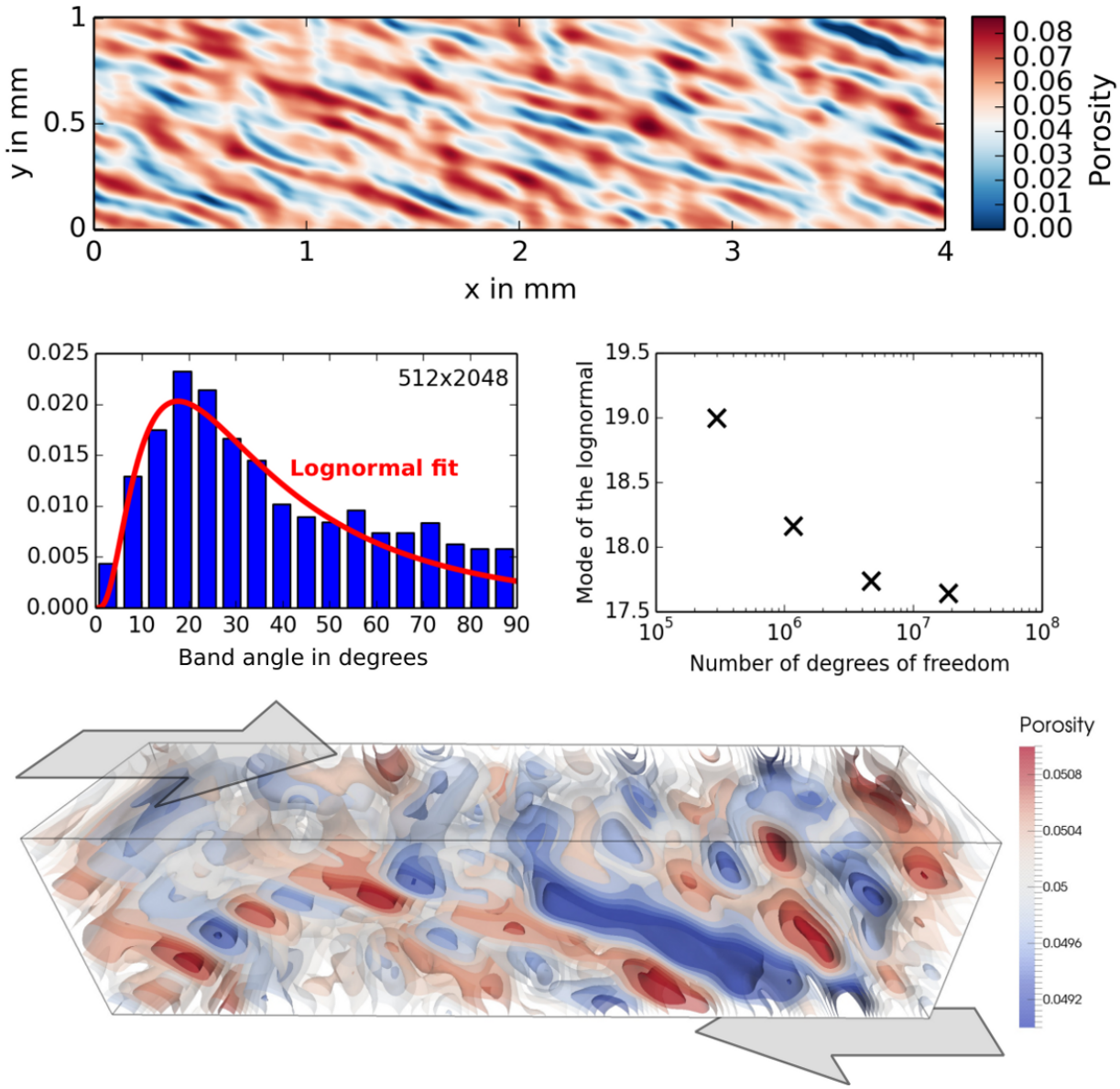

FIGURE 4. *Band angle of magmatic shear bands after a strain of* $\gamma = 1$. *(top) Porosity field after the final time step for a model with* 512×2048 *cells. (middle left) Histogram of the band angle distribution of the model shown at the top after binning in 5-degree intervals. The red line shows the best fit of a log-normal distribution to the band angle distribution. (middle right) Dominant band angle (i.e. mode of the log-normal distribution shown on the left) for models with different resolution, showing convergence to a value of* $\approx 17.5°$. *(bottom) Shear bands in three dimensions.*

TABLE 3. Parameters and scaling used for the shear bands, plume and global convection model.

Quantity	Shear bands model	Plume model	Global convection model
ξ_0	1.41176×10^8 Pa s	5^{18} Pa s	10^{19} Pa s
η_0	1.41176×10^7 Pa s	5^{19} Pa s	5^{21} Pa s
η_f	100 Pa s	10 Pa s	10 Pa s
ρ_{s_0}	3000 kg/m^3	3400 kg/m^3	3400 kg/m^3
ρ_{f_0}	3000 kg/m^3	3000 kg/m^3	3000 kg/m^3
k_0	5×10^{-9} m^2	5^{-9} m^2	10^{-8} m^2
n_{dis}	6	–	–
ϕ_0	0.05	0.05	– $\quad (\xi \sim e^{\alpha\phi})$
α	-27	-10	-10
β	–	5	7
α_{thermal}	–	3.5×10^{-5} 1/K	2×10^{-5} 1/K
T_{ref}	–	1600 K	1600 K
k_{thermal}	–	4.7 W/(m K)	4.7 W/(m K)
κ_s	–	3.2×10^{-12} 1/Pa	4.2×10^{-12} 1/Pa
κ_f	–	3.8462×10^{-11} 1/Pa	1.25×10^{-11} 1/Pa
$\frac{\partial \kappa_f}{\partial p}$	–	1.6	0
X extent	0.004 m	600 km	8700 km
Z extent	0.001 m	300 km	2900 km
u_s	$(\pm 32\text{m yr}^{-1}, 0)$	–	–
γ	1	–	–
CFL	1	1	1
n_x	128, 256, 512, 1024, 2048	adaptive (128–512)	adaptive (64–512)

averaged products $\rho_{f,s}\,\mathbf{u}_s$ as well as $\rho_{f,s}\,\mathbf{g}$ are constant, but the divergence of the velocity is not zero:

$$
\begin{aligned}
\mathbf{u}_s(x,z) &= (0.1e^z, -0.075e^z),\\
\rho_s(x,z) &= 1.2e^{-z},\\
\rho_f(x,z) &= e^{-z},\\
\mathbf{g}(x,z) &= (0, -e^z),
\end{aligned}
$$

which also leads to all the terms $\frac{\nabla\rho}{\rho}$ being constant. The remaining material parameters are constructed to create a zero horizontal component of the fluid pressure, a vertical component that depends only on z, and to satisfy our previous

assumption that $\frac{\nabla\rho}{\rho} \approx \kappa\rho\mathbf{g}$:

$$\begin{aligned}
\eta(x,z) &= \frac{1}{2}e^{2x},\\
\xi(x,z) &= e^{-z} + \frac{2}{3}e^{2x} + 1,\\
K_D(x,z) &= \frac{149}{45} + \frac{1}{30}e^{z},\\
\kappa_s &= \frac{5}{6},\\
\kappa_f &= 1,\\
\Gamma &= \frac{1}{37}e^{z},
\end{aligned}$$

This leads to the following solution for the porosity, fluid pressure, compaction pressure and fluid velocity:

$$\begin{aligned}
\phi(x,z) &= 1 - 0.3e^{z},\\
\nabla p_f &= (0, -0.135e^{z} - 1),\\
p_c(x,z) &= 0.075\xi e^{-z},\\
\mathbf{u}_f(x,z) &= (0.1e^{z}, -0.075e^{z} - 2.2\frac{K_D}{\phi}e^{z}).
\end{aligned}$$

The results are shown in Figure 5. In the top part, velocity u and porosity ϕ are converging as expected with order $k+1$ in the L^2 norm, except that we can not explain why u for $k = 2$ is only converging quadratically (but the correct order is attained when discretizing with $k = 3$). The melt velocity is computed as a postprocess from u and the gradient of the pressure solutions, which explains the almost linear convergence order. This is not a problem in practice, because the melt velocity is not used in the computation and is only used for visualization. The bottom half of Figure 5 shows convergence of the three pressures with optimal orders. Altogether, these results demonstrate the functionality and accuracy of our solver for the fully compressible formulation of two-phase flow.

4.4. **Adaptive convergence.** To demonstrate the effectiveness of adaptive mesh refinement when applied to problems of melt migration, we have set up a test case with an incompressible, analytical solution featuring a vein of high porosity standing out against a low-porosity background (Figure 6), and including a compaction viscosity with a Gaussian in the middle of the domain. We constructed the boundary conditions, the source term and the gravity in such a way that the the solution is:

$$\begin{aligned}
\phi &= 0.01 + 0.2\exp\left(-20(x+2z)^2\right),\\
\xi &= 0.1 + 0.1\exp\left(1 - 20(x^2+z^2)\right),\\
K_D &= \phi,\\
\mathbf{u}_s &= (x, e^{z} - z),\\
p_s &= 1 - z,\\
p_c &= -\xi\nabla\cdot u = -0.1e^{z} - 0.1e^{z}\exp\left(1 - 20(x^2+z^2)\right).
\end{aligned}$$

A script to generate the constructed material parameters, source terms and boundary conditions can be found in the supplementary material.

In this example we use a refinement criterion employing a gradient jump estimator based on the porosity and the compaction pressure. An example mesh can be seen in Figure 7 and the refinement clearly captures the region of interest for the two fields in the estimator. Note that the refinement does not match the features of the velocity or solid

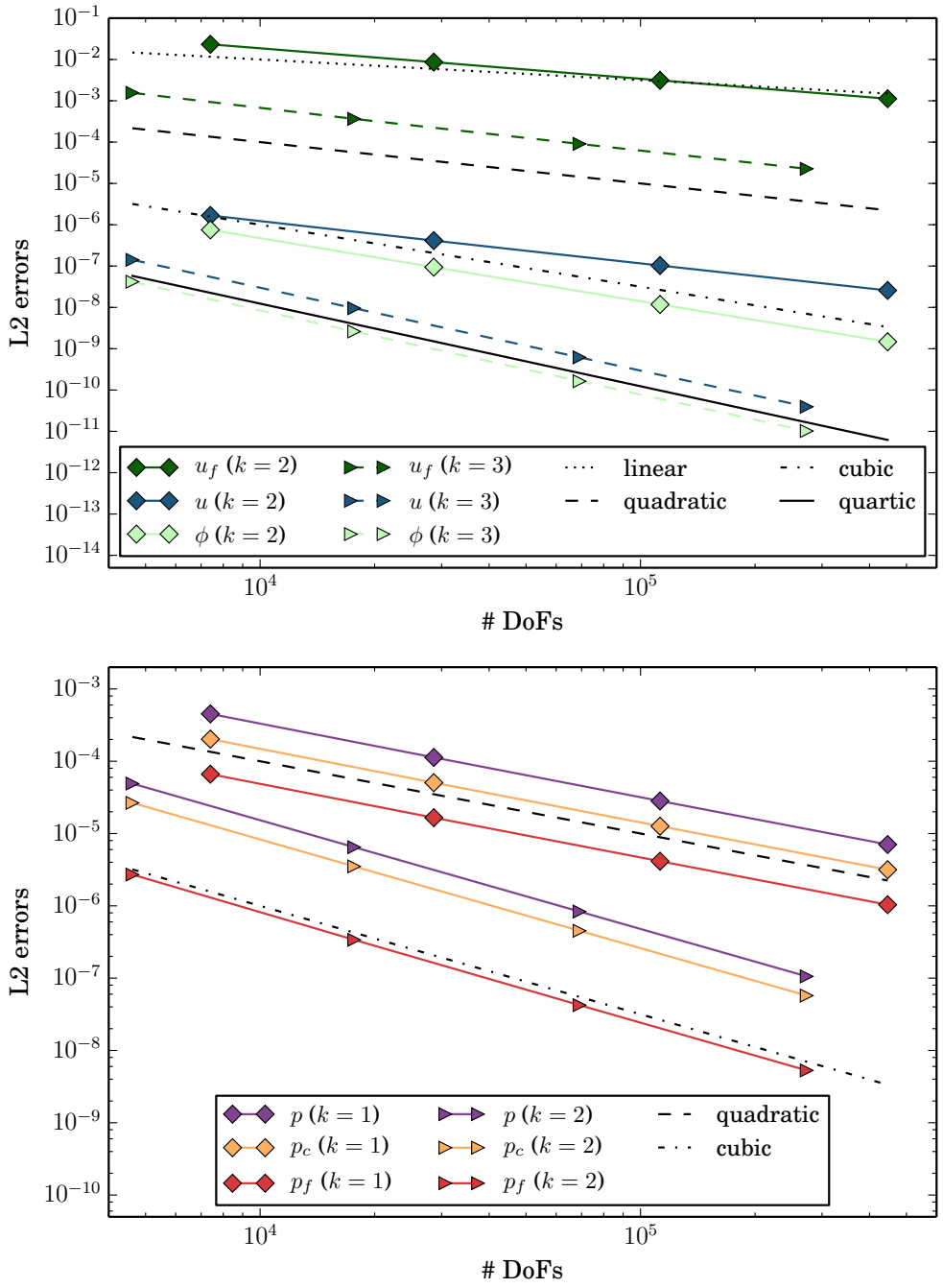

FIGURE 5. *Results of spatial convergence test for different polynomial degrees k (diamonds: $Q_2 \times Q_1$, triangles: $Q_3 \times Q_2$) Plotted are the L2 errors relative to the compressible, 2D, analytical solution. Linear, quadratic, cubic and quartic trends are shown for reference as dotted and dashed lines.*

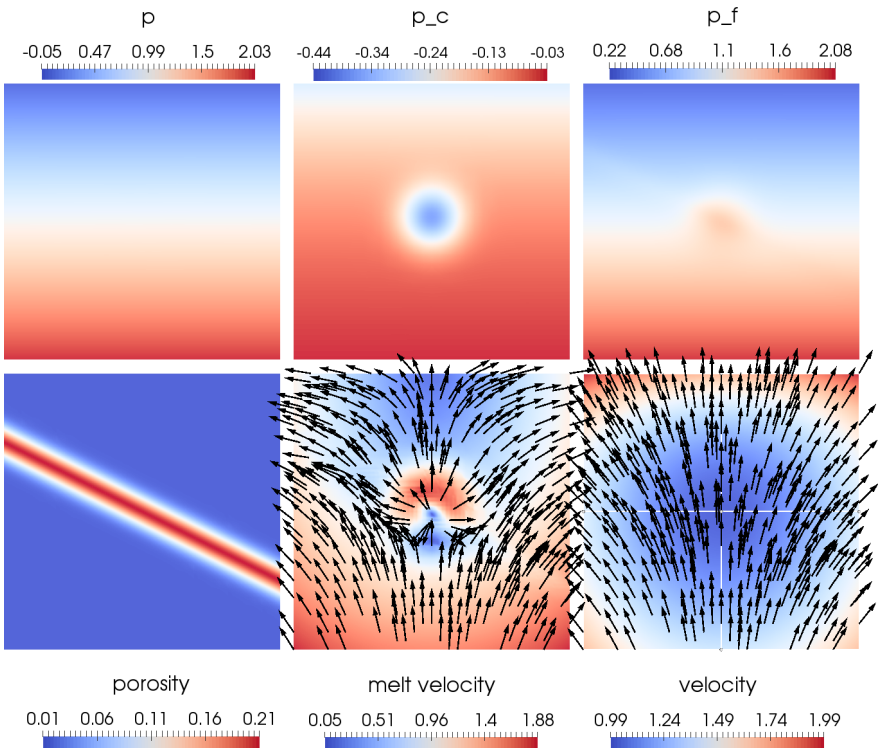

FIGURE 6. *Setup of the convergence test for adaptive mesh refinement. Top row is solid pressure, compaction pressure, and fluid pressure. Bottom row shows porosity, melt velocity, and solid velocity. The main feature is a vein of increased porosity standing out against a low-porosity background.*

pressure, so we can not expect superior performance compared to global refinement. While it would have been easy to improve the adaptive convergence by changing the setup to concentrate the features of every variable in the vein, we think this is a more realistic setup. Even then, the improvements in the error over global refinement are convincing and highlight how useful adaptive refinement in the setting of melt migration can be, see Figure 8.

In this model global refinement requires two to four times as many degrees of freedom compared to adaptive refinement (for quantities like compaction pressure, porosity, and derived quantities like melt velocity). While quantities like solid velocity see no improvement here, the errors are very small to begin with because the field is relatively smooth compared to the melt velocity. This is likely also true for most realistic problems. For realistic models we propose to combine one of these criteria with refinement based on other solution variables or material properties such as temperature or viscosity.

4.5. **Melt transport in a rising mantle plume.** When hot buoyant material in form of a mantle plume approaches the surface, the temperatures inside of the plume exceed the solidus and material starts to melt. We use this example as an application for our coupled magma/mantle dynamics code. We present two- and three-dimensional plume models, and employ both the incompressible and compressible formulation of two-phase flow. The model domain is a Cartesian box, extending from the Earth's surface to 300 km depth and 600 km horizontally. The initial temperature profile is adiabatic with a potential temperature of 1600 K, with a cold top thermal boundary layer corresponding to oceanic lithosphere with an age of 10 million years and a top temperature of 293 K. A spherical perturbation of 250 K with a diameter of 80 km is added in the center of the bottom boundary of the model to start the plume ascent. Initially, there

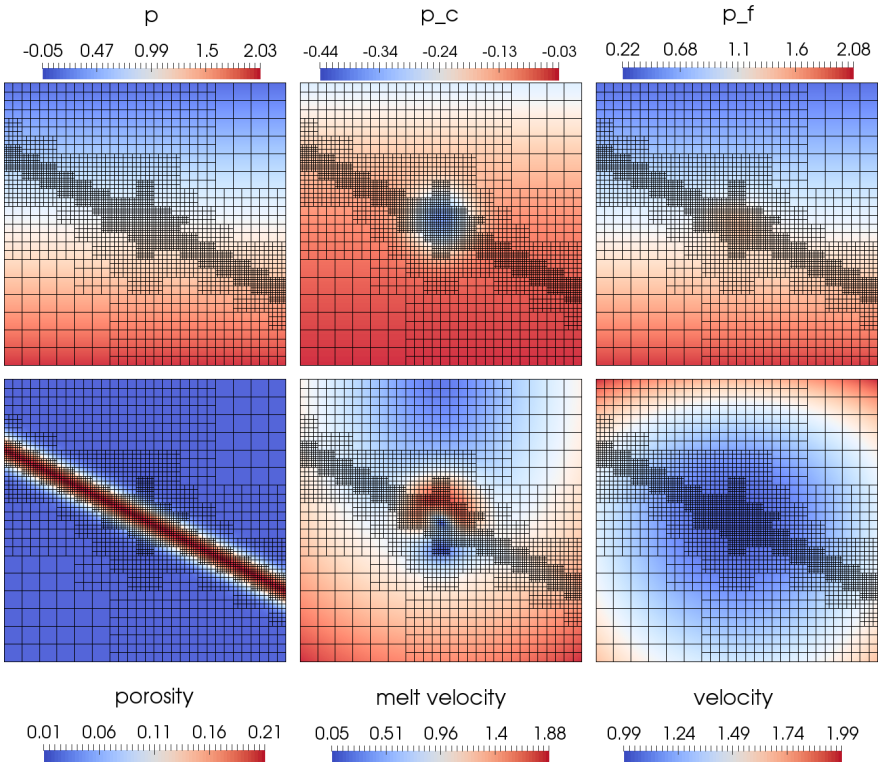

FIGURE 7. *Fields like in Figure 6, but showing the mesh refined using an error indicator based on a combination of porosity and compaction pressure gradient jumps. The algorithm clearly detects the peak in the compaction pressure and the vein and resolves them using small cells.*

is no porosity present in the model. The temperature boundary conditions are prescribed according to the initial values at top and bottom, and insulating at the sides; the velocity boundary conditions are free slip everywhere except for the bottom boundary layer, where the hydrostatic pressure is applied, but material is allowed to flow in and out. This leads to inflow of hot material acting as a plume tail. The rheology is purely Newtonian, but both shear and compaction viscosity are temperature- and porosity-dependent in the form

$$\eta(\phi, T) = \eta_0 e^{\alpha(\phi-\phi_0)} e^{-\beta(T-T_0)/T_0}, \tag{32}$$

$$\xi(\phi, T) = \xi_0 \frac{\phi_0}{\phi} e^{-\beta(T-T_0)/T_0}, \tag{33}$$

with exponents of $\alpha = -5$ and $\beta = 10$, which are chosen lower compared to what experiments suggest to limit the viscosity contrast in the model to approximately 6 orders of magnitude. The melting parametrization [16] is described in Appendix A. We apply no freezing of melt here, as we are mainly interested in how the volume of generated melt evolves over time and the related differences between the compressible and incompressible formulation. However, latent heat of melting is incorporated, with an entropy change of $\Delta S = -300$ J/(kg K) upon melting.

In this setting, the porosity can exceed values of 25–35%, where the host rock ceases to be a connected matrix and starts to disaggregate into individual blocks and grains. It has been argued [17] that Darcy flow can still be a valid approximation for this type of flow, in this case describing the settling and interaction of a mush or single grains of solid in the melt phase. The permeability is then a measure for how much the relative flux of one phase is hindered by

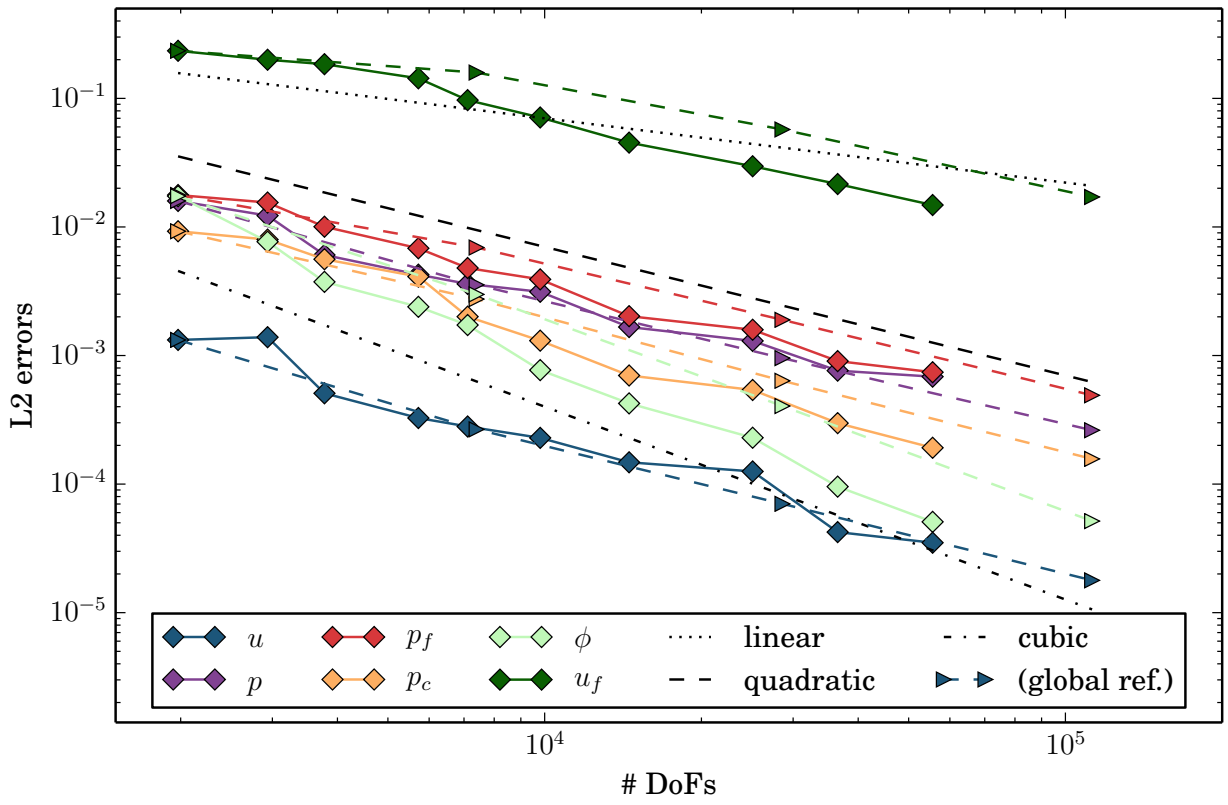

FIGURE 8. *Convergence plot of L2 errors of various quantities with adaptive refinement (solid lines with diamonds) compared to global refinement (dashed lines with triangles). As expected from the refinement in the porosity vein, the errors for porosity, compaction pressure, and fluid velocity are clearly superior, while other errors are comparable to global refinement. Linear, quadratic and cubic trends are shown for reference as dotted and dashed lines.*

the other phase. We follow the approach of Keller et al. [17] and use the parametrized permeability law

$$k_\phi = k_0 \phi^n (1-\phi)^m \qquad \text{with } n = 3 \text{ and } m = 2. \tag{34}$$

To test the influence of considering the individual compressibility of solid and fluid on the model evolution, we performed models with three different formulations of the density parametrization (Figure 9a):

(1) with constant melt and solid densities $\rho_f = 3000\,\text{kg/m}^3$ and $\rho_s = 3400\,\text{kg/m}^3$, only depending on temperature,
(2) pressure- and temperature-dependent densities, with the solid density fit to PREM [10] and the melt density fit to data for komatiite melts [1] using a dependency in the form $\rho = \rho_0(1 - \alpha_{\text{thermal}}(T - T_{\text{adi}}))e^{\kappa p}$, but incompressible formulation of the mass and momentum conservation equation,
(3) the same densities as in (2), but with the fully compressible system of equations.

A comprehensive list of model parameters can be found in Table 3, and except for the properties mentioned above the material model is the same as described in Section 4.2.

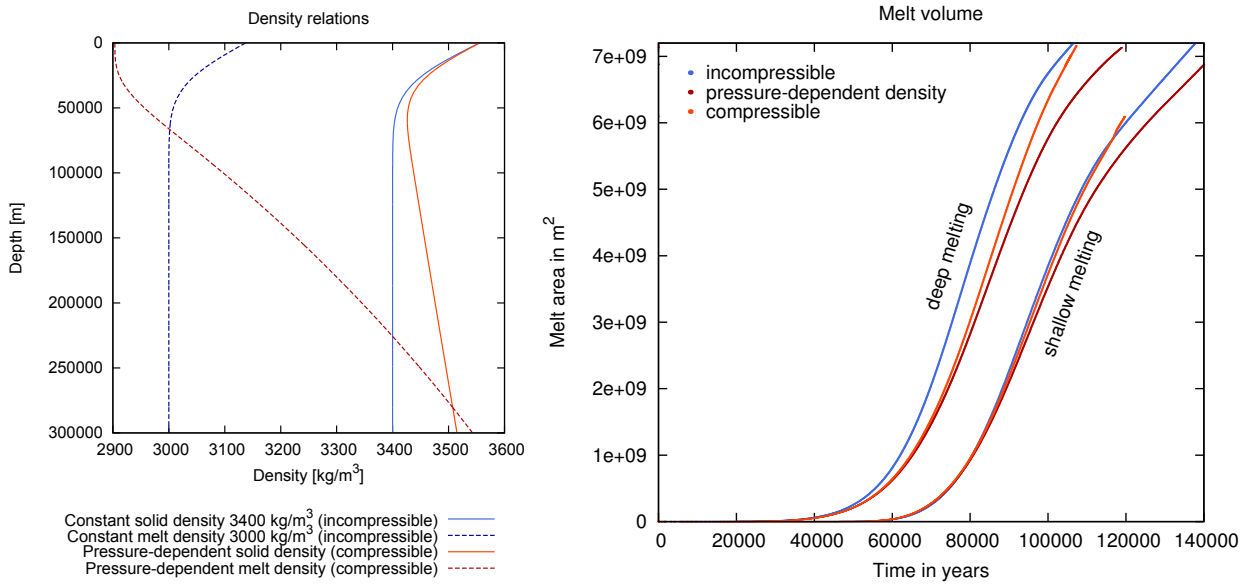

FIGURE 9. *Buoyancy and melt volume in a rising mantle plume.* ***(left)*** *Density profiles used for the different plume models: Solid lines denote solid density, dashed lines denote melt density. Colors illustrate the density formulation: Blue lines mark a density that only depends on temperature, but not on pressure, red lines mark both temperature- and pressure-dependent densities.* ***(right)*** *Development of melt volume over time in dependence of the employed density formulation. Blue lines mark a model where both solid and melt phase are individually incompressible, and the density does not depend on pressure (blue density profiles on the left, purely incompressible formulation); dark red lines mark a model where both solid and melt phase are individually incompressible, but the density depends on pressure (red density profiles on the left, this is analogue to the extended Boussinesq approximation for Stokes flow); and light red lines mark a model where both solid and melt phase are individually compressible and the density depends on pressure (red density profiles on the left, full compressible formulation). The two sets of lines mark different melting parameterizations, leading to melt production in different depth regions of the mantle.*

During the model evolution, the plume ascends from the bottom of the model due to its high buoyancy. At a pressure of approximately 5 GPa material starts to melt, lowering the viscosities and further reducing the density. While the plume rises, the melt first accumulates at its top until it reaches a depth of 50 km, where the melt starts to separate from the plume head, moving further up and spreading laterally at the base of the lithosphere (Figure 10). In agreement with previous studies of melt migration in mantle plumes with lower melt fractions [27], melt segregation velocities point almost vertically upwards, and within the plume head magnitudes of melt and solid velocities are comparable. Horizontal movement occurs when melt is advected with the solid plume material (for low melt fractions) and as it stagnates below the impermeable lithosphere in a melt-rich layer. The generated shear initiates small-scale downwellings of cold and dense lithosphere above into the low-viscosity plume material, leading to mixing in the plume head and thinning of the lithosphere. The full model evolution is shown in Supplementary Movie S2. We evaluate the volume of generated melt over the model evolution time and compare this quantity between the different setups (Figure 9b).

In the purely incompressible model, the density of the melt is very low, leading to a fast plume ascent and earlier melting and upwards migration of melt. In the models with pressure-dependent density, the buoyancy of the plume is smaller, and the plume rises more slowly. This explains the faster growth of melt volume for the purely incompressible model. However, there is also a volume difference between the compressible case and the incompressible, but pressure-dependent density case. As there is no difference in density parameterizations between these models, the plume buoyancy, melt generation rate and ascent velocity is identical. But as the compressible formulation considers the extension of the melt phase when it reaches lower pressures, a higher overall melt volume is reached in this model. The difference in melt volume between these two cases depends on the melt compressibility, but it is also influenced by where and how much melt is generated, i.e. the melting parametrization. For melt generated at greater pressures, the change in density and thus the volume change is higher. For the example cases shown here it amounts to 5% in the case with shallow melting and 11.4% in the case with deep melting. As the models are only two-dimensional, these values technically represent melt areas, and not melt volumes, so that for a three-dimensional model an even stronger effect of compressibility (of $\Delta V \approx \Delta A^{3/2}$) is expected, leading to differences of up to 18%.

Figure 11 shows a model with identical setup as in the incompressible case, but in three dimensions, and illustrates how melt accumulates at the top of the rising plume head. It also demonstrates how a combination of static and adaptive mesh refinement can be used to resolve features of interest while saving computational resources: the mesh is refined statically in a cylinder around the plume and in the lithosphere, and in addition to that is refined adaptively where melt is present.

4.6. **Influence of melt migration on a global convection model.** After showcasing our implementation on a realistic example of melt migration in a rising mantle plume, we will demonstrate that with the aid of adaptive mesh refinement our software also allows it to combine models of global mantle convection and melt migration. We study how melt generation and segregation impact the dynamics of such a model by comparing a classic mantle convection model – where only the equilibrium melt fraction in dependence of temperature and pressure is computed – and a model with coupled magma/mantle dynamics, where melt is allowed to migrate. More precisely, we consider the distribution of melt, the flow field, and average velocities and temperatures.

As our focus is on the qualitative influence of melt migration on the model dynamics, we simplify the model setup to only include basic features important to study this dependence. We choose a Cartesian geometry with an aspect ratio of three and dimensions of 2900×8700 km. The model is heated from the bottom and cooled from the top, with no additional heat sources in the form of internal heating, latent heat or shear heating. We employ a simplified melting parametrization with a linear dependence of the solidus temperature on pressure p and depletion C, and assume that the generated melt is proportional to the temperature in excess of the solidus:

$$\phi_{\text{equilibrium}} = \frac{T - T_{\text{sol}}}{T_{\text{liq}} - T_{\text{sol}}} \qquad \text{with } T_{\text{sol}} = T_{\text{sol,0}} + \Delta T_p\, p + \Delta T_c\, C \tag{35}$$

$$T_{\text{liq}} = T_{\text{sol}} + 500 \text{ K} \tag{36}$$

$$T_{\text{sol,0}} = 1300 \text{ K} \tag{37}$$

$$\Delta T_p = 6 \times 10^{-8} \text{ K/Pa} \tag{38}$$

$$\Delta T_c = 200 \text{ K} \tag{39}$$

The melting rate is computed as the difference between the equilibrium melt fraction and the melt present in the model. While these melting relations are strongly simplified, they capture the qualitative influence of temperature, pressure and depletion/enrichment on the melting rate and are an appropriate approximation for studying the general model behavior with the present melt fractions of up to 20% and the dependence of melt generation and migration on the model dynamics. Whenever melt is generated in the model and migrates upwards, it leaves behind depleted material, and when the porosity present in the model exceeds the computed equilibrium melt fraction, melt freezes, creating enriched material. This change in material composition is modeled by a density change of the material proportional to

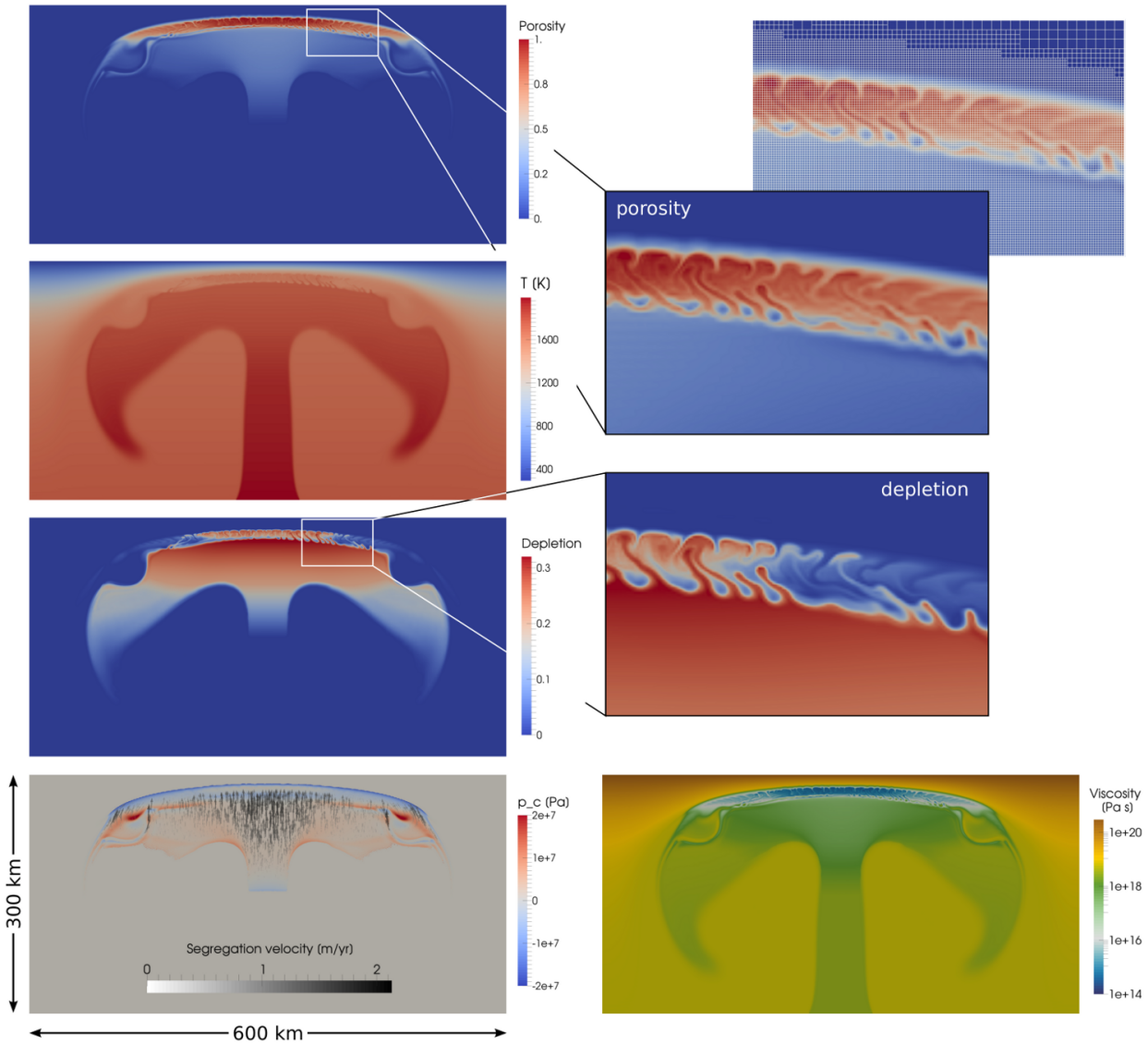

FIGURE 10. *Dynamics of melt migration in a rising mantle plume. Snapshots of melt fraction (also showing the finite element mesh), depletion, temperature, compaction pressure, segregation velocity (difference between melt and solid velocity) and viscosity in the plume after a model time of* $t = 142000$ *years as it spreads below the lithosphere (incompressible model). During the plume ascent, melt accumulates at the top of the plume head and starts to separate from the melting region when the plume approaches the base of the lithosphere and spreads laterally. Interaction with the cold lithosphere leads to small-scale convection and mixing inside of this lens of molten material. An animation of the plume ascent is provided in Supplementary Movie S2.*

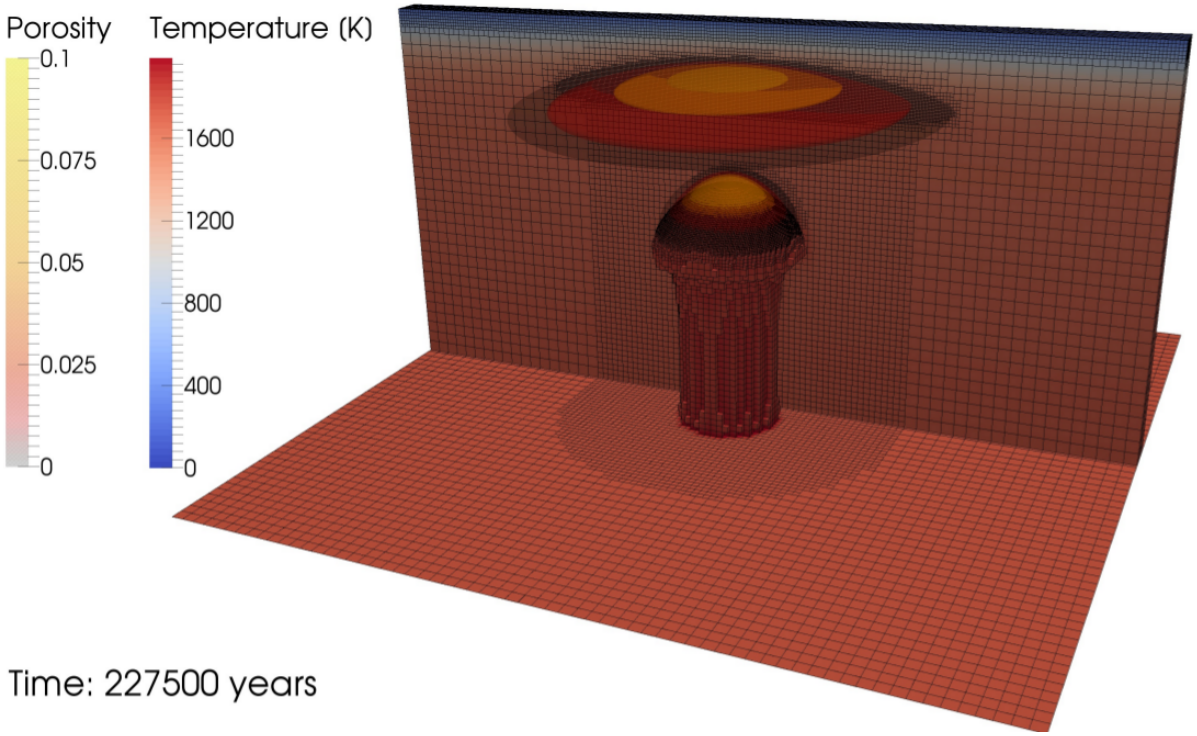

FIGURE 11. *Temperature, porosity and mesh in a three-dimensional model of melt migration in a rising mantle plume. Background colors represent temperature, contours show porosity. The mesh is refined towards the center of the plume, in the top boundary layer and adaptively in regions where melt is present.*

enrichment/depletion, with depleted material being less dense and enriched material being denser than the surrounding mantle. In addition, porosity weakens the material as described in Section 4.5, except for the compaction viscosity, which follows an exponential dependence equivalent to the one for the shear viscosity. All model parameters can be found in Table 3.

In the classic mantle convection model (Figure 12, top), melt is generated by decompression melting where hot material reaches a shallow depth and partially molten areas remain relatively stationary as long as the general pattern of the flow field does not change. In the model with melt migration (Figure 12, bottom), the same mechanism of melt generation is active, initially leading to melting in the same regions where hot material is upwelling and approaching the surface. However, as the melt migrates upwards, it reaches regions with lower ambient mantle temperatures and starts to freeze, leaving behind depleted material that is not fertile enough to generate new melt. This means that the overall melt volume is much smaller (Figure 13, bottom left), as is expected for fractional melting in comparison to batch melting. Moreover, patches of enriched material created by freezing of melt influence the model dynamics: as it has a higher density than the surrounding mantle, cold and enriched material sinks down, initiating several small downwellings that do not occur in the model without melt migration. Figure 13 (top) illustrates the evolution of enrichment and depletion over time: As soon as melt is generated in the model, it migrates upwards from its source, where it freezes again, creating a layer of enriched material close to the top of the model, and leaving behind a layer of depleted material below, in 200 – 400 km depth. In principle, even though the model is extremely simplified, these

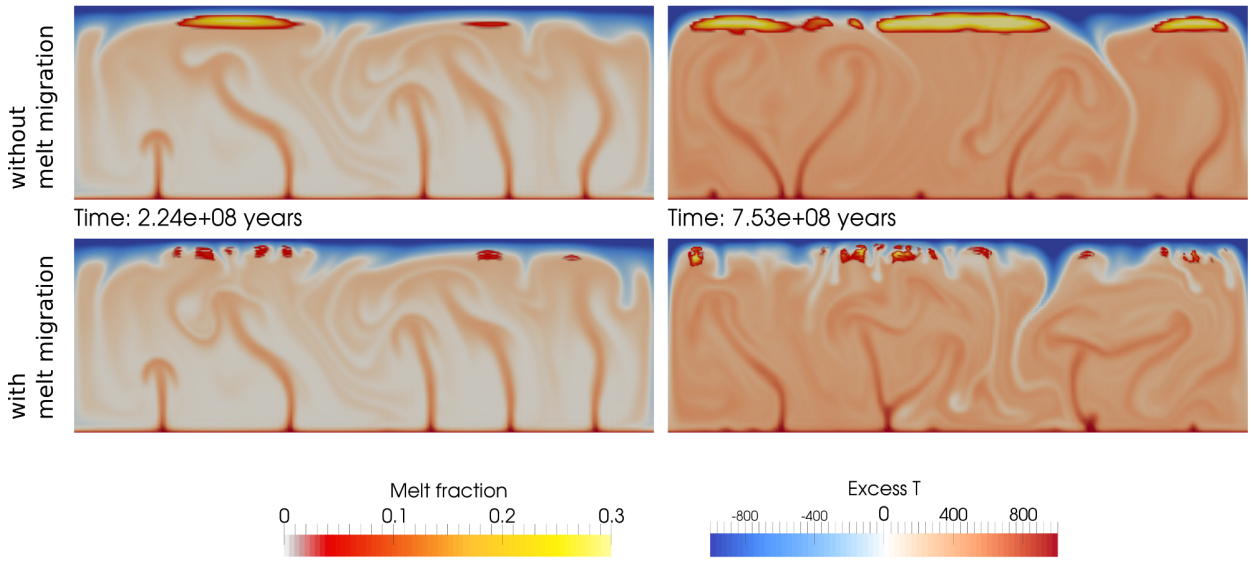

FIGURE 12. *Time snapshots of temperature and melt fraction in global models with melt migration. The upper row shows a model without melt migration, where the melt fraction is calculated as postprocessor for the present temperature and pressure conditions (i.e. batch melting), the lower row shows a model with melt migration (and fractional melting). Columns are different points in time. The model without melt migration features broad patches of melt, generated in regions of upwelling in the model. In contrast, the model with melt migration shows several smaller patches of melt with downwellings in between, where the lithosphere is eroded due to the destabilizing effect of the high-density, crystallized material. Different average temperatures are due to the fact that the model initial conditions are not the steady state values, but due to the model geometry (i.e. box domain and 2D) the equilibrium conditions would not reflect realistic temperatures for the Earth.*

layers correspond to the Earth's crust (or at least the part of the crust generated by plumes, as there are no divergent plate boundaries in the model where oceanic crust and lithosphere would be generated) and the asthenosphere. Of course, the melt does not migrate through the previously existing cold top layer in our models and hence can not reach the surface. However, the small-scale convection initiated by the downwellings of dense enriched, crystallized material allows for new, hot material to flow upwards, and melt intruding further upwards into the lithosphere. This is already a similar process as what is described by Sobolev et al. [32] as thermo-magmatic erosion of the lithosphere by mantle plumes. The downwelling enriched material is subsequently distributed over the whole model domain (blue streaks towards the end of the time evolution in 13, top).The full model evolution is presented in Supplementary Movie S3.

This diverging model dynamics is also visible in the root mean square velocities (Figure 13, bottom right): During the first 250 million years both models behave almost identically, but afterwards different peaks develop in the two models. However, as the root mean square velocity is mainly influenced by upwellings instead of downwellings (due to the lower viscosities) both the average value and the frequency of peaks remain similar.

It is very likely that the model behavior will change if a more complex melting and material behavior is incorporated, but our model shows that already this very simple approximation of melting, together with melt migration, has a strong influence on the model dynamics, including average model velocities, predicted melt volumes and number and frequency of downwellings.

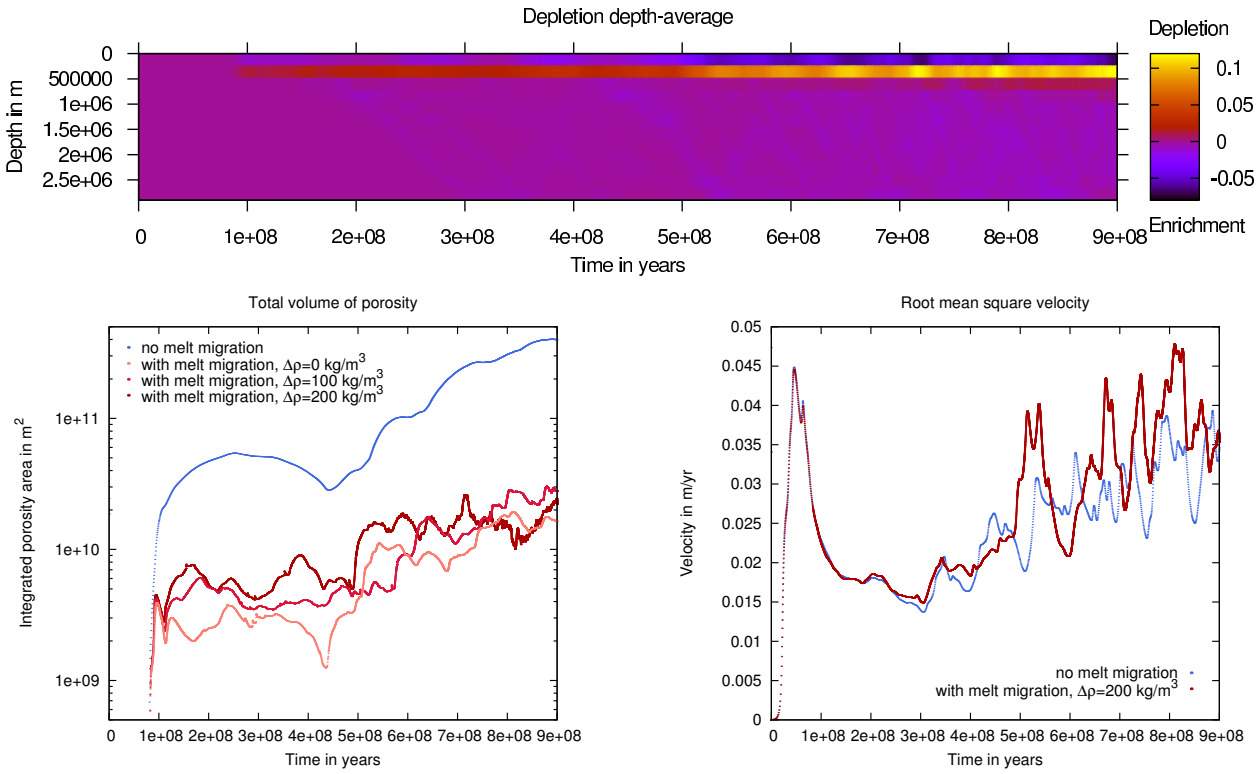

FIGURE 13. *Time evolution of global models with melt migration.* ***(top)*** *Depletion field, depth-averaged in 12 slices. Once melt starts to be generated, enriched material accumulates in the top layer, and depleted material in a layer below in 200 – 400 km depth. Part of the enriched material also flows downwards and is distributed over the whole model domain.* ***(bottom left)*** *Development of the melt volume for models with (red lines) and without (blue line) melt migration, and varying density contrasts between "enriched" and "depleted" material. For the model without melt migration, melt volume is calculated as equilibrium melt fraction for the present temperature and pressure conditions (i.e. batch melting).* ***(bottom right)*** *Development of the root mean square velocity for models with (red line) and without (blue line) melt migration. While the model evolution is similar in the beginning, it diverges once a significant amount of melt is generated (compare left side), and the model with melt migrations shows higher velocity peaks.*

5. CONCLUSIONS AND OUTLOOK

In this study, we described how to implement two-phase flow in two and three dimensions in a finite element code with adaptive mesh refinement. The proposed formulation, which includes the compressibility of the individual solid and melt phase in addition to compaction, allows models to be extended consistently to greater depth in the Earth's mantle. The presented applications demonstrate the accuracy and efficiency of our software and its ability to capture the behavior of melt in relevant application cases of magma/mantle dynamics on different scales, ranging from millimeters to thousands of kilometers. Simulations of mantle plumes and global convection show that including melt migration in a model significantly changes the convection pattern, and for deep melts the compressibility can have an effect of an order of 20% on the computed melt volume. The main advantages of the presented method

are (1) the effectiveness of adaptive mesh refinement, allowing for higher resolution or larger model domains with the same computational resources, (2) the potential to study applications with three-dimensional geometries and (3) the capability to couple melt migration to processes deeper in the Earth's mantle and global mantle convection in a consistent formulation considering the compressibilities of solid and melt phase.

Despite all this, the methods described here are not sufficient to solve all conceivable models related to melt migration realistically: The focus of this study is on the coupling of magma dynamics to mantle dynamics on larger scales, and our current approach does not consider elastic and plastic deformation of the material. Hence, it does not allow for modeling of melt transport through fractures or dikes, one of the main modes of melt extraction on smaller scales such as in the lithosphere and crust [17]. These deformation mechanisms introduce additional non-linearities and make the problem numerically challenging, demanding the use of more efficient non-linear solvers, ideally employing Newton's method, to be viable in three dimensions.

In addition, we here concentrate on the mechanical evolution of the two-phase system, simplifying its thermal and chemical evolution and using parameterizations for calculating melting and freezing rate and the influence of melt on material properties. This approximation considers the qualitative influence of compositional changes on solidus, liquidus, density, viscosity and other material properties. However, it does not allow an accurate computation of the melt and residuum composition in a multicomponent system or the associated chemical heterogeneities generated by the melting process – which would be required for a more realistic description of the rheology of partially molten regions and a more sophisticated comparison of the model to geochemical data. Employing thermodynamic data to calculate melting rates self-consistently and keeping track of the evolution of solid and melt composition should be a goal for future modeling studies.

Finally, we assume that melt and solid are always in thermodynamic equilibrium. However, this might not be a valid approximation for all applications of porous flow in the Earth's mantle and excludes modeling disequilibrium melting such as described in Rudge et al. [24]. Geochemical evidence suggests that the melts that formed mid-ocean ridge basalts were not in chemical equilibrium with the matrix they were migrating through; and modeling has shown that disequilibrium is important for the formation of reactive instabilities, leading to melt focusing and channelized flow below mid-ocean ridges [35].

Nevertheless, we have shown that ASPECT can be applied to a number of relevant model setups for coupled magma/mantle dynamics and that it has the potential to become a versatile and useful tool for the magma migration community.

5.1. **Acknowledgments.** Both authors were partially supported by the Computational Infrastructure for Geodynamics initiative (CIG), through the National Science Foundation under Award No. EAR-0949446 and The University of California – Davis. T. Heister was partially supported by National Science Foundation grant DMS1522191. J. Dannberg acknowledges the support of the Helmholtz graduate research school GeoSim.

Most of the computational resources were provided by the North-German Supercomputing Alliance (HLRN) as part of the project "Plume-Plate interaction in 3D mantle flow – Revealing the role of internal plume dynamics on global hot spot volcanism". Clemson University is acknowledged for generous allotment of compute time on Palmetto cluster.

REFERENCES

[1] Agee, C. B. & Walker, D., 1993. Olivine flotation in mantle melt, *Earth and Planetary Science Letters*, **114**(23), 315 – 324.

[2] Ballmer, M. D., Ito, G., Wolfe, C. J., & Solomon, S. C., 2013. Double layering of a thermochemical plume in the upper mantle beneath hawaii, *Earth and Planetary Science Letters*, **376**, 155 – 164.

[3] Bangerth, W., Burstedde, C., Heister, T., & Kronbichler, M., 2011. Algorithms and data structures for massively parallel generic adaptive finite element codes, *ACM Trans. Math. Softw.*, **38**(2).

[4] Bangerth, W., Heister, T., et al., 2015. *ASPECT: Advanced Solver for Problems in Earth's ConvecTion*, `https://aspect.dealii.org/`.

[5] Bangerth, W., Heister, T., Heltai, L., Kanschat, G., Kronbichler, M., Maier, M., Turcksin, B., & Young, T., 2015. The dealii library, version 8.2, *Archive of Numerical Software*, **3**(1).

[6] Barcilon, V. & Lovera, O. M., 1989. Solitary waves in magma dynamics, *Journal of Fluid mechanics*, **204**, 121–133.

[7] Barcilon, V. & Richter, F. M., 1986. Nonlinear waves in compacting media, *Journal of Fluid mechanics*, **164**, 429–448.

[8] Cagnioncle, A.-M., Parmentier, E. M., & Elkins-Tanton, L. T., 2007. Effect of solid flow above a subducting slab on water distribution and melting at convergent plate boundaries, *Journal of Geophysical Research: Solid Earth*, **112**(B9), B09402.

[9] Dannberg, J. & Heister, T., 2015. Supporting computer code, https://github.com/jdannberg/aspect/tree/melt_reorder_fields.

[10] Dziewonski, A. M. & Anderson, D. L., 1981. Preliminary reference earth model, *Physics of the Earth and Planetary Interiors*, **25**(4), 297 – 356.

[11] Gerya, T., 2011. Future directions in subduction modeling, *Journal of Geodynamics*, **52**(5), 344 – 378.

[12] Holtzman, B. K. & Kohlstedt, D. L., 2007. Stress-driven melt segregation and strain partitioning in partially molten rocks: Effects of stress and strain, *Journal of Petrology*, **48**(12), 2379–2406.

[13] Katz, R. F., 2006. The dynamics of melt and shear localization in partially molten aggregates, *Nature*, **442**, 676–679.

[14] Katz, R. F., 2008. Magma dynamics with the enthalpy method: Benchmark solutions and magmatic focusing at mid-ocean ridges, *Journal of Petrology*, **49**(12), 2099–2121.

[15] Katz, R. F., 2010. Porosity-driven convection and asymmetry beneath mid-ocean ridges, *Geochemistry, Geophysics, Geosystems*, **11**(11), Q0AC07.

[16] Katz, R. F., Spiegelman, M., & Langmuir, C. H., 2003. A new parameterization of hydrous mantle melting, *Geochemistry, Geophysics, Geosystems*, **4**(9), 1073.

[17] Keller, T., May, D. A., & Kaus, B. J. P., 2013. Numerical modelling of magma dynamics coupled to tectonic deformation of lithosphere and crust, *Geophysical Journal International*, **195**(3), 1406–1442.

[18] Kronbichler, M., Heister, T., & Bangerth, W., 2012. High accuracy mantle convection simulation through modern numerical methods, *Geophysical Journal International*, **191**(1), 12–29.

[19] McKenzie, D., 1984. The generation and compaction of partially molten rock, *Journal of Petrology*, **25**(3), 713–765.

[20] Mittelstaedt, E., Ito, G., & van Hunen, J., 2011. Repeat ridge jumps associated with plume-ridge interaction, melt transport, and ridge migration, *Journal of Geophysical Research: Solid Earth (1978–2012)*, **116**(B1).

[21] Ohtani, E. & Maeda, M., 2001. Density of basaltic melt at high pressure and stability of the melt at the base of the lower mantle, *Earth and Planetary Science Letters*, **193**(12), 69 – 75.

[22] Rhebergen, S., Wells, G. N., Katz, R. F., & Wathen, A. J., 2014. Analysis of block preconditioners for models of coupled magma/mantle dynamics, *SIAM Journal on Scientific Computing*, **36**(4), A1960–A1977.

[23] Rhebergen, S., Wells, G. N., Wathen, A. J., & Katz, R. F., 2015. Three-field block preconditioners for models of coupled magma/mantle dynamics, *SIAM Journal on Scientific Computing*, **37**(5), A2270–A2294.

[24] Rudge, J. F., Bercovici, D., & Spiegelman, M., 2011. Disequilibrium melting of a two phase multicomponent mantle, *Geophysical Journal International*, **184**(2), 699–718.

[25] Ruedas, T., Schmeling, H., Marquart, G., Kreutzmann, A., & Junge, A., 2004. Temperature and melting of a ridge-centred plume with application to iceland. part i: Dynamics and crust production, *Geophysical Journal International*, **158**(2), 729–743.

[26] Sanloup, C., Drewitt, J. W. E., Konopkova, Z., Dalladay-Simpson, P., Morton, D. M., Rai, N., van Westrenen, W., & Morgenroth, W., 2013. Structural change in molten basalt at deep mantle conditions, *Nature*, **503**, 104–107.

[27] Schmeling, H., 2000. Partial melting and melt segregation in a convecting mantle, in *Physics and Chemistry of Partially Molten Rocks*, pp. 141–178, Springer.
[28] Schmeling, H., 2010. Dynamic models of continental rifting with melt generation, *Tectonophysics*, **480**(14), 33 – 47.
[29] Schmeling, H. & Marquart, G., 2008. Crustal accretion and dynamic feedback on mantle melting of a ridge centred plume: The iceland case, *Tectonophysics*, **447**(14), 31 – 52, Plate movement and crustal processes in and around Iceland.
[30] Scott, D. R. & Stevenson, D. J., 1986. Magma ascent by porous flow, *Journal of Geophysical Research B*, **91**(B9), 9283–9296.
[31] Simpson, G. & Spiegelman, M., 2011. Solitary wave benchmarks in magma dynamics, *Journal of Scientific Computing*, **49**(3), 268–290.
[32] Sobolev, S. V., Sobolev, A. V., Kuzmin, D. V., Krivolutskaya, N. A., Petrunin, A. G., Arndt, N. T., Radko, V. A., & Vasiliev, Y. R., 2011. Linking mantle plumes, large igneous provinces and environmental catastrophes, *Nature*, **477**(7364), 312–316.
[33] Spiegelman, M., 1996. Geochemical consequences of melt transport in 2-d: The sensitivity of trace elements to mantle dynamics, *Earth and Planetary Science Letters*, **139**(1), 115–132.
[34] Spiegelman, M., 2003. Linear analysis of melt band formation by simple shear, *Geochemistry, Geophysics, Geosystems*, **4**(9), 8615.
[35] Spiegelman, M., Kelemen, P. B., & Aharonov, E., 2001. Causes and consequences of flow organization during melt transport: The reaction infiltration instability in compactible media, *J. geophys. Res*, **106**(B2), 2061–2077.
[36] Stevenson, D. J., 1989. Spontaneous small-scale melt segregation in partial melts undergoing deformation, *Geophysical Research Letters*, **16**(9), 1067–1070.
[37] Suzuki, A. & Ohtani, E., 2003. Density of peridotite melts at high pressure, *Physics and Chemistry of Minerals*, **30**(8), 449–456.
[38] Weatherley, S. M. & Katz, R. F., 2012. Melting and channelized magmatic flow in chemically heterogeneous, upwelling mantle, *Geochemistry, Geophysics, Geosystems*, **13**(5), Q0AC18.
[39] Wiggins, C. & Spiegelman, M., 1995. Magma migration and magmatic solitary waves in 3-d, *Geophysical Research Letters*, **22**(10), 1289–1292.

APPENDIX A. PARAMETRISATION OF THE MELTING MODEL

Modeling of melt generation requires a parametrization for the melting rate in dependence of temperature, pressure and composition. We use the parametrization from Katz et al. [16] for melting of dry peridotite (Figure 14).

In addition, when material undergoes the phase transition from solid to fluid (or the other way round), latent heat is consumed (or released). The effects of latent heat are included in the energy conservation equation in form of the term $\rho_s T \Delta S \left(\frac{\partial F}{\partial t} + \mathbf{u}_s \cdot \nabla F\right)$. Here, ΔS is the change of entropy (positive for exothermic phase transitions) and F is the degree of depletion (the fraction of the source rock that has already been molten; without melt extraction from the source this is equal to the melt fraction). As the phase of the material, for a given composition, depends on the temperature and pressure, the latent heat term can be reformulated:

$$\begin{aligned}\frac{\partial F}{\partial t} + \mathbf{u}_s \cdot \nabla F &= \frac{DF}{Dt} \\ &= \frac{\partial F}{\partial T}\frac{DT}{Dt} + \frac{\partial F}{\partial p_s}\frac{Dp_s}{Dt} \\ &= \frac{\partial F}{\partial T}\left(\frac{\partial T}{\partial t} + \mathbf{u}_s \cdot \nabla T\right) + \frac{\partial F}{\partial p_s}\mathbf{u}_s \cdot \nabla p_s.\end{aligned}$$

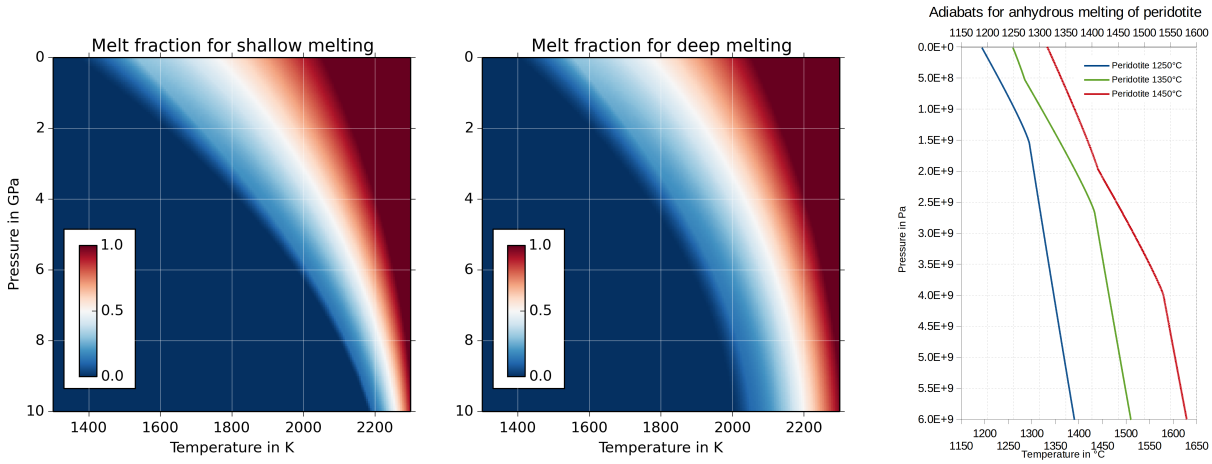

FIGURE 14. *Melt fraction in dependence of temperature and pressure after Katz et al. [16, left] and modified for deep melting (middle), and temperature profile of adiabatically upwelling material when latent heat of melting is taken into account for batch melting of anhydrous peridotite. Parameterizations after Katz et al. [16].*

The last transformation results from the assumption that the flow field is always in equilibrium and consequently $\partial p/\partial t = 0$. This means, we have to calculate the partial derivatives of our melt fraction parametrization with respect to temperature and pressure.

A.1. **Melting of peridotite prior to the exhaustion of clinopyroxene.** For peridotite, there are two different functions prior to and after the exhaustion of clinopyroxene. Prior to the exhaustion of clinopyroxene

$$
\begin{aligned}
F(p,T) &= \left(\frac{T - T_{\text{sol}}(p)}{T^{\text{lh}}_{\text{liq}}(p) - T_{\text{sol}}(p)}\right)^{\beta} \\
\frac{\partial F(p,T)}{\partial T} &= \beta \left(\frac{T - T_{\text{sol}}(p)}{T^{\text{lh}}_{\text{liq}}(p) - T_{\text{sol}}(p)}\right)^{\beta-1} \frac{1}{T^{\text{lh}}_{\text{liq}}(p) - T_{\text{sol}}(p)} \\
\frac{\partial F(p,T)}{\partial p} &= \beta \left(\frac{T - T_{\text{sol}}(p)}{T^{\text{lh}}_{\text{liq}}(p) - T_{\text{sol}}(p)}\right)^{\beta-1} \\
&\qquad \left(\frac{\partial T^{\text{lh}}_{\text{liq}}(p)}{\partial p}(T_{\text{sol}}(p) - T) + \frac{\partial T_{\text{sol}}(p)}{\partial p}(T - T^{\text{lh}}_{\text{liq}}(p))\right) \frac{1}{(T^{\text{lh}}_{\text{liq}}(p) - T_{\text{sol}}(p))^2}
\end{aligned}
$$

with the solidus $T_{\text{sol}}(p) = A_1 + A_2 p + A_3 p^2$,
the lherzolite liquidus $T^{\text{lh}}_{\text{liq}}(p) = B_1 + B_2 p + B_3 p^2$
and the true liquidus $T_{\text{liq}}(p) = C_1 + C_2 p + C_3 p^2$.

A.2. **Melting of peridotite after the exhaustion of clinopyroxene.** The exhaustion of clinopyroxene happens at the melt fraction

$$F_{\text{cpx-out}} = \frac{M_{\text{cpx}}}{R_{\text{cpx}}(p)} \quad \text{with} \quad R_{\text{cpx}}(p) = r_0 + r_1 p$$

TABLE 4. Parameters used for melting of anhydrous peridotite. Modified from Katz et al. [16].

Parameter	Used for	Value	Value for deep melting	Unit
A_1	T_{sol}	1085.7	1120.7	K
A_2		$1.329 \cdot 10^{-7}$	$1.1 \cdot 10^{-7}$	K Pa^{-1}
A_3		$-5.1 \cdot 10^{-18}$	$-5 \cdot 10^{-18}$	K Pa^{-2}
B_1	$T_{\text{liq}}^{\text{lh}}$	1475.0		K
B_2		$8.0 \cdot 10^{-8}$		K Pa^{-1}
B_3		$-3.2 \cdot 10^{-18}$		K Pa^{-2}
C_1	T_{liq}	1780.0		K
C_2		$4.5 \cdot 10^{-8}$		K Pa^{-1}
C_3		$-2.0 \cdot 10^{-18}$		K Pa^{-2}
β	F	1.5		
M_{cpx}		0.15		mass fraction
r_0		0.5		mass fraction
r_1		$8 \cdot 10^{-11}$		mass fraction Pa^{-1}
ΔS	latent heat	-300		J kg^{-1} K^{-1}

and marks a change in the productivity of the system. M_{cpx} is the mass fraction of clinopyroxene in the peridotitic host rock and R_{cpx} is the reaction coefficient for cpx in the melting reaction. For $F > F_{\text{cpx-out}}$

$$
\begin{aligned}
F(p,T) &= F_{\text{cpx-out}} + (1 - F_{\text{cpx-out}}) \left(\frac{T - T_{\text{cpx-out}}(p)}{T_{\text{liq}}(p) - T_{\text{cpx-out}}(p)} \right)^{\beta} \\
\frac{\partial F(p,T)}{\partial T} &= \beta(1 - F_{\text{cpx-out}}) \left(\frac{T - T_{\text{cpx-out}}(p)}{T_{\text{liq}}(p) - T_{\text{cpx-out}}(p)} \right)^{\beta-1} \frac{1}{T_{\text{liq}}(p) - T_{\text{cpx-out}}(p)} \\
\frac{\partial F(p,T)}{\partial p} &= \frac{\partial F_{\text{cpx-out}}}{\partial p} \left[1 - \left(\frac{T - T_{\text{cpx-out}}(p)}{T_{\text{liq}}(p) - T_{\text{cpx-out}}(p)} \right)^{\beta} \right] \\
&\quad + \beta(1 - F_{\text{cpx-out}}) \left(\frac{T - T_{\text{cpx-out}}(p)}{T_{\text{liq}}(p) - T_{\text{cpx-out}}(p)} \right)^{\beta-1} \\
&\quad \frac{\frac{\partial F_{\text{cpx-out}}}{\partial p}(T_{\text{cpx-out}}(p) - T_{\text{liq}}(p)) + \left(\frac{\partial T_{\text{liq}}}{\partial p} - \frac{\partial T_{\text{cpx-out}}}{\partial p} \right)(T_{\text{cpx-out}}(p) - T)}{(T_{\text{liq}}(p) - T_{\text{cpx-out}}(p))^2}
\end{aligned}
$$

with $T_{\text{cpx-out}} = F_{\text{cpx-out}}{}^{\frac{1}{\beta}} \left[T_{\text{liq}}^{\text{lh}}(p) - T_{\text{sol}}(p) \right] + T_{\text{sol}}(p)$.

A.3. **Parameters.** The parameters used for the solidus and liquidus temperatures and the melt fraction are taken from Katz et al. [16] for the case of anhydrous melting and are given in Table 4. For modeling melting under higher pressures, such as shown in Section 4.5 (deep melting), we modified the solidus temperature (reflecting a compositional change or change in volatile fraction), resulting in the deepest melts in the plume being generated in approximately 230 km depth.

A.4. **Validation.** We test our melting model by computing the numerical solution for the temperature profile of adiabatically upwelling material that undergoes melting and the associated latent heat effects. Figure 14 (right) shows these results, which can be compared to equivalent data for anhydrous melting in Katz et al. [16, figure 11b], who

calculate a simplified version of the productivity function

$$\left.\frac{dF}{dP}\right|_S = \frac{-\frac{c_p}{T}\left.\frac{\partial T}{\partial P}\right|_F + F\frac{\alpha_f}{\rho_f} + (1-F)\frac{\alpha_s}{\rho_s}}{\Delta S + \frac{c_p}{T}\left.\frac{\partial T}{\partial F}\right|_P} \tag{40}$$

and then numerically integrate

$$\left.\frac{dT}{dP}\right|_S = \frac{T}{c_p}\left(F\frac{\alpha_f}{\rho_f} + (1-F)\frac{\alpha_s}{\rho_s} + \Delta S\left.\frac{dF}{dP}\right|_S\right) \tag{41}$$

to receive the P-T path of the adiabat.

APPENDIX B. SUPPLEMENTARY MOVIES

The provided animations show the development of several of the presented models:

Movie S1. Animation of the development of magmatic shear bands in three dimensions in a partially molten host rock that is exposed to shearing. Setup, colors and scaling are the same as in Figure 4 (bottom). The animation can also be found at https://www.youtube.com/watch?v=zOEqhaiBswU.

Movie S2. Animation of the evolution of a rising mantle plume that undergoes melting. Setup, colors and scaling are the same as in Figure 10. The animation can also be found at https://youtu.be/aWndYbMIjVQ.

Movie S3. Animation of the evolution of a global mantle convection model that incorporates melting, illustrating the difference between only computing melt fractions (top) and allowing melt to migrate and influence the model behavior (bottom). Setup, colors and scaling are the same as in Figure 13. The animation can also be found at https://youtu.be/Kwyp4Jvx6MU.